OPTICAL PROPERTIES OF PLASMONIC NANOSTRUCTURES FOR BIO-IMAGING AND BIO-SENSING APPLICATIONS

by

VIRA V. KRAVETS

B.S., Physics, Taras Shevchenko National University of Kyiv, Ukraine, 2007

M.S., Physics, Taras Shevchenko National University of Kyiv, Ukraine, 2009

A thesis submitted to the Graduate Faculty of the

University of Colorado Colorado Springs

in partial fulfillment of the

requirements for the degree of

Doctor of Philosophy

Department of Physics

2017

This dissertation for the Doctor of Philosophy degree by

Vira V. Kravets

has been approved for the

Department of Physics

by

Anitoliy Pinchuk, Chair

Kevin Tvrdy

Karen Livesey

Kathrin Spendier

Robert Camley

Date 05/11/2017

Kravets, Vira V. (Ph.D., Physics)

Optical Properties of Plasmonic Nanostructures for Bio-imaging and Bio-sensing Applications

Dissertation directed by Associate Professor Anatoliy Pinchuk.

ABSTRACT

This dissertation explores the physics of free electron excitations in gold nanoparticle chains, silver nanoparticle colloids, and thin gold films. Electron excitations in nanostructures (surface plasmons, SP) are responsible for unique optical properties, which are applied in bio-sensing and bio-imaging applications.

For gold nanoparticle chains, the effect of SP on resonance light absorption was studied experimentally and theoretically. Mainly, how the spectral position of the absorption peak depends on inter-particle distances. This dependence is used in "molecular rulers", providing spatial resolution below the Rayleigh limit. The underlying theory is based on particle interaction via scattered dipole fields. Often in literature only the near-field component of the scattered field is considered. Here, I show that middle and far fields should not be neglected for calculation of extinction by particle chains.

In silver nanoparticles, SP excitations produce two independent effects: (a) the intrinsic fluorescence of the particles, and (b) the enhancement of a molecule's fluorescence by a particle's surface. The mechanism of (a) is deduced by studying how fluorescence depends on particle size. For (b), I show that fluorescence of a dye molecule on the surface of a nanoparticle is enhanced, when compared to that of the free-standing dye. I demonstrate that the dye's fluorescent quantum yield is dependent

on the particle's size, making labeled silver nanoparticles attractive candidates as bio-imaging agents. Labeled nanoparticles are applied to cell imaging, and their bio-compatibility with two cell lines is evaluated here.

Finally, in gold films under attenuated total internal reflection (ATR) conditions, the SP create a propagating wave (SP-polariton, SPP) when coupled with the incident light. Because of the sensitivity of SPPs to the medium adjacent to the gold film surface, they are widely applied in bio-sensing applications. A toolbox for the description of sputter-deposited gold films is presented here: it employs three experimental techniques (ATR, transmittance and atomic force microscopy) in combination with the effective medium theory for double-layered film model. Our findings have allowed for the avoidance of superficial fitting parameters in our model.

This dissertation is dedicated to my beloved sister, Nina

ACKNOWLEDGMENTS

I would like to take a moment and express my gratitude to my collaborators, role models, teachers, friends and family for guiding, support, and for walking side-by-side with me on a path towards Ph.D.

My gratitude goes to my adviser, Dr. Anatoliy Pinchuk who opened a world of international research to me, introduced me to Argonne National Lab, and supported me when I for the first time presented in front of a large audience of at the international conferences.

I also would like to thank Dr. Robert Camley, Dr. Karen Livesey, and Dr. Kathrin Spendier, who always had great advice, helped to believe in myself as a scientist, and contributed enormously to my progress towards Ph.D. I thank to my fellow students Jason Nobles, and Dr. Nick Anderson for being a great support during our graduate classes together.

And of course, I thank to my family: Nina, Irina, and Natalia, who held my hand through ups and downs of this road. They were always by my side, even as we were thousands of miles away. I thank to all my friends from the climbing, yoga, and dancing communities of Colorado Springs, who became my second family, and made this city feel like home.

TABLE OF CONTENTS

CHAPTER

CHAPTER I

INTRODUCTION

1.1 Introduction to plasmonics

In this dissertation, I aim to detail the optical properties of *plasmonic* nanostructures and their applications in bio-sensing and bio-imaging. I combine experiment and theory to investigate strong extinction in chains of gold nanoparticles (with explanation of potential molecular ruler application); photoluminescence of glycine-dimer-coated silver nanoparticles (with demonstration of their use in fluorescent imaging of neural stem and rat basophilic leukemia cells); and attenuated total internal reflection in gold films (with demonstration in sensing of immunoglobulin E and other molecules).

Materials which exhibit collective oscillations of free electrons (*plasmons*) are said to be *plasmonic*. Gold and silver (studied in this dissertation), as well as copper are some of the most well studied plasmonic materials. Although plasmonic effects have been known for more than a century, the field of *plasmonics* [1] has recently seen rapid growth due to advances in nanofabrication and numerous applications of plasmons in medicine, [2] photovoltaics, [3] biosensing, [4] to name just a few. Studies involving methods of manipulating nanoscale structures for enhanced field concentration (squeezing light into sub-wavelength structures) is at the heart of current plasmonic research. [5,6,7]

The first theoretical works for description of surface plasmons go as far back as 1908, when Mie showed why sharp absorption bands (providing colors to stained glass) depend on the particle's size. [8] Mie applied Maxwell's electromagnetic theory to

spherical particles. For extensive background on plasmonics I refer my reader to M. Born and E. Wolf's "Principles of Optics" published in 1980, and "Absorption and scattering of light by small particles" by C.F. Bohren and D.R. Huffman, 1983.

Nowadays plasmonic nanostructures with different shapes, sizes, configurations, embedding media etc. are available, due to advances in electron beam lithography, ion beam patterning, sputter- and electron-beam- deposition, chemical synthesis, and other high precision nanofabrication techniques. And, therefore it is time to test existing theoretical models to see how well they fit the mentioned variety. In Chapter 2 I address theoretical approach to the extinction in arrays of near-spherical gold nanoparticles, manufactured with electron beam lithography, and challenge a wide-spread assumption of the *near-field only* interaction between the neighboring particles.

There are multiple benefits to study *nano*-structures (sizes of ~10^{-9} meters), as opposed to micro- or bulk metal structures. I will name just a few:

- on the nanoscale, plasmons emerge on a *surface* of the nanostructure, manifesting themselves through unique optical properties (no such pronounced optical properties exist neither on micro-scale, nor in bulk materials); [9]

- surface plasmons in nanoparticles are excited directly by light, as opposed to bulk plasmons, which cannot be excited by light. And, in certain geometries, propagating surface plasmons within the thin metal films can also be excited by light. [10,11]

Among unique optical properties, mentioned above, focus of this dissertation is going to be on polarization- and inter-particle-distance-dependent extinction in chains of gold nanoparticles (Chapter 2), size-dependent photoluminescence and extinction of silver nanoparticles (Chapter 3), and morphology-dependent attenuated total internal

reflection in gold nano-films (Chapter 4). More in-depth motivation and background for each optical property of the nanostructures of interest are described below. For completeness, I note that some parts of this dissertation have previously been published, as listed in Appendix A.

1.2 Motivation for the study of chains of gold nanoparticles

Nanoparticle (NP) chains are widely used as biosensors and molecular rulers [12,13], in plasmonics, [14,15] nanooptics, [7,16] photovoltaics, [17] and biochemistry. [18] When the frequency of incident light the matches frequency of a surface plasmon in a NP, *surface plasmon resonance* (SPR) is observed. The principle behind sensing with surface plasmons is based on high sensitivity of SPR modes to the NP's environment. [19] It can be observed via optical spectroscopy: namely the maximum of the extinction spectrum, which corresponds to SPR wavelength, shifts because of a molecule attachment to a NP. [20]

Over the last decade, interest has turned from NP ensemble's SPR (such as colloidal NPs) towards the SPR in a *single nanoparticle*. [21] However, a high degree of sensor miniaturization tends to result in a worse detection limit: the number of molecules interacting with the single nanoparticle is not enough to achieve a good signal-to-noise ratio with a simple optical setup. A solution lies in the use of an array of plasmonic NPs, each of which can resolve molecule binding events. In addition to increased sensitivity, arrays bring selectivity, since their optical properties also depend on the inter-particle disctance and orientation of polarization of the incoming light with respect to the array. Recently Kravets V.G. et al. showed that the sensitivity of ordered-nanoparticles-array-based sensors can be an order of magnitude higher than that of conventional sensors. [13]

In Chapter 2 I present experimental and theoretical studies of NP chains with different inter-particle distances. These chains assembled into arrays (for better signal-to-noise ratio), with large (one micron) inter-chain distance. Large inter-chain distance allows avoidance of interactions between the chains (for simplicity of a model). Each chain consists of near-spherical gold nanoparticles of 50 nm diameter and height. I study how extinction of light passing through the arrays depends on inter-particle distance and on light polarization. Results of this study can be used for bio-sensing, molecular ruler, waveguiding applications, present first of a kind optical extinction map, which includes broad range of inter-particle distances and polarizations.

While sensing is the most popular application of NP chains, application in molecular rulers is also very promissing. I further discuss how polarization- and distance-dependent maps can be used in label-free molecular rulers. The main purpose of a molecular ruler is to precisely resolve distance between objects, below diffraction limit. [22] For example, if one places NPs at a distance less than 200 nm apart, it is impossible to distinguish whether there is one, or several particles with conventional microscopy tools (due to the Rayleigh limit), unless, NPs are interacting in such a way, that their optical properties are sensitive to the inter-particle distance. Some molecular rulers are based on DNA-functionalized NPs, where the distance between the particles is determined by the DNA length. [12] A simpler label-free molecular ruler, described in this work, can be an alternative for super-resolution purposes.

The principle of application of our NP chains in a ruler is based on the fact that frequency of oscillation of free electrons in a NP *within a chain* is different, compared to frequency of oscillation in an *individual NP*. The chain-SPR is shifted spectrally with

respect to the individual-NP-SPR, and is detectable with dark field microscopy (Figure 1), extinction spectroscopy (our method of choice, Chapter 2), and other optical techniques.

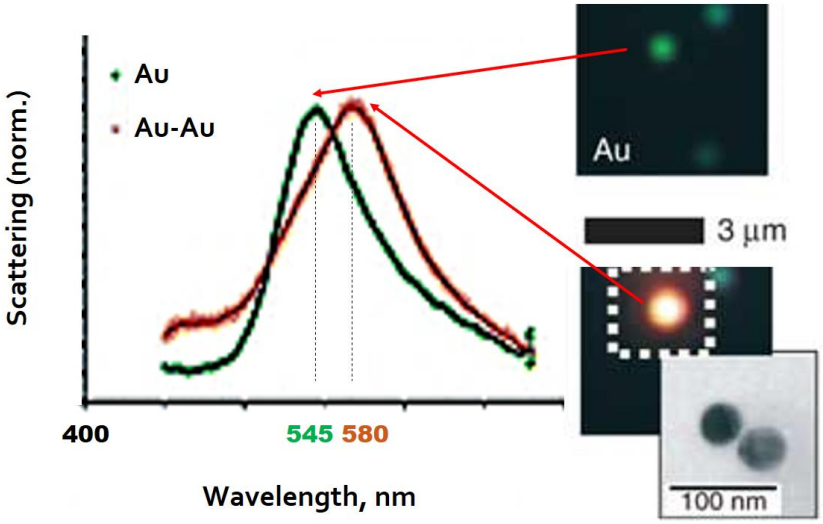

Figure 1. Dark field scattering spectra for individual gold NP (green), and two interacting gold NPs (red). Inset shows electron microscopy image for two particles. Adapted by permission from Macmillan Publishers Ltd: [NATURE BIOTECHNOLOGY], *[12]* copyright (2005).

In optical microscopy and spectroscopy, the wavelength is used more often than frequency to describe light, hence I will be talking about SPR wavelength for this matter. To understand why the SPR wavelength shifts spectrally, one can imagine free electrons within a particle as simple harmonic oscillator, acted upon with the driving force of an incident light (Drude model). [23] The electron oscillations, which are in resonance with the incident light wave (SPR), are very sensitive to the inter-particle distance. Such sensitivity is a result of their interaction via dipole fields, scattered by particles (black semi-circles on Figure 2). Dipole fields create additional forces (directed as E_{dip} on Figure 2), acting on neighboring particles in a chain. Vector addition of these forces to

the force of polarization (directed as E_{pol} on Figure 2) can either enhance, or dampen driving force of the incident electromagnetic field (directed as induced dipoles, p on Figure 2).

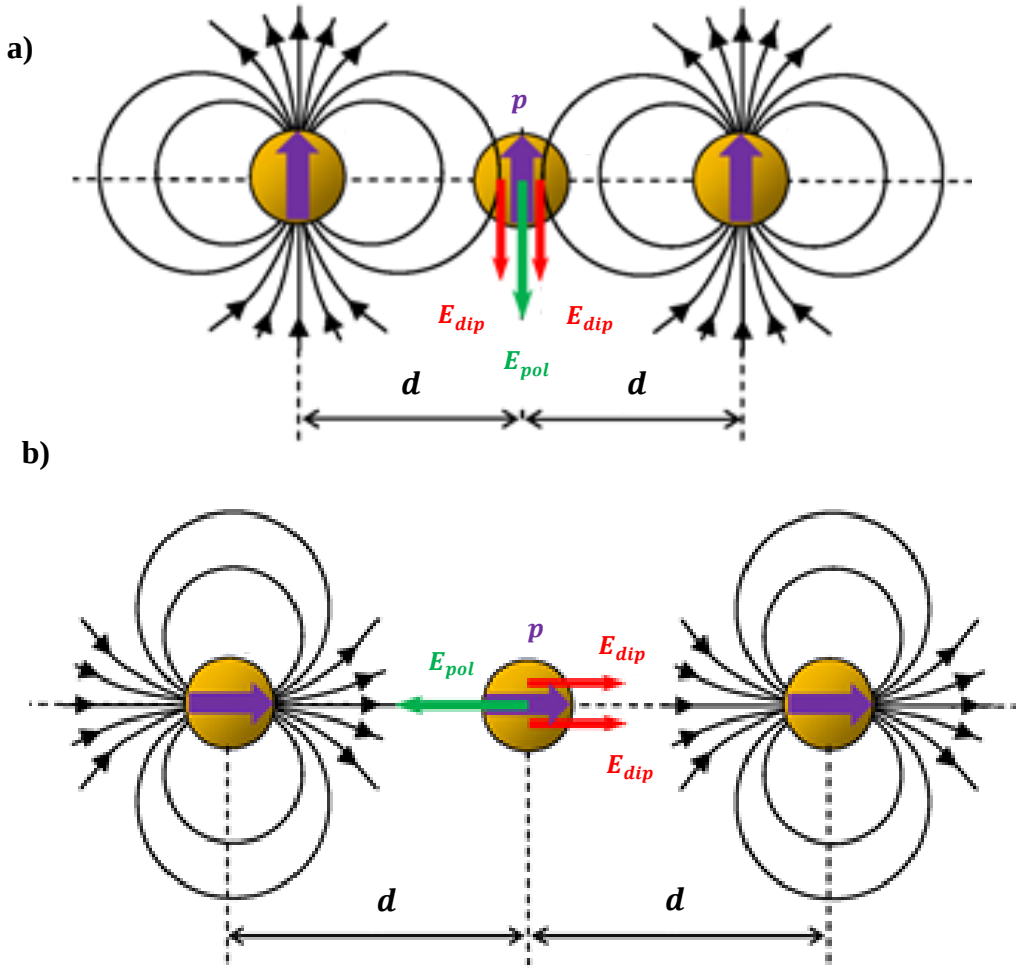

Figure 2 .Electromagnetic coupling between spherical nanoparticles for small distances between the particles ($d << \lambda$): (a) the SPR oscillations are perpendicular to the axis of the chain (s-polarization); (b) parallel to the axis (p-polarization). Induced dipoles denoted by p, are in the same direction as the incident electric field.

Whether driving force will be enhanced or damped, depends on the orientation of the chain axis with respect to the incident light polarization (Figure 2 (a) vs (b)). One can

describe this interaction between neighboring particles by saying that the SPR mode in a chain of particles is *coupled*. [24]

The nature of the electromagnetic coupling depends on the distance *d* between the NPs. Specifically, at large distances coupling is retarded, and at small distances (and by small distance I mean distance between the NPs is smaller than wavelength of incident electromagnetic wave, $d << \lambda$) the coupling is assumed quasi-electrostatic (frequency dependence is incorporated in dielectric function of a metal, but not into the form of an incident field. Hence, the dipole fields are in phase with the incident field). It is often called near-field interaction.

Let's first consider short distances. For s-polarized light (Figure 2 (a)), where the incident electromagnetic wave has electric field perpendicular to the chain axis. The way dipole fields, E_{dip}, add with the polarization field, E_{pol}, in the central particle determines if collective SPR wavelength will be greater or less than the SPR wavelength of an individual NP. Since all three fields (red arrows and a green arrow) are in the same direction, *opposite* to the incident electric field (directed as a purple arrow), the resultant field in the central particle is *weakened*. And, therefore electrons in this particle experience a weaker driving force, compared to the case of an individual NP. A weaker force leads to a lower SPR frequency (therefore, red shift of collective SPR wavelength). In summary, for s-polarized light, collective SPR wavelength is greater than individual SPR wavelength.

At the same time, for p-polarized light (Figure 2 (b)) the driving (incident) wave has electric field parallel to the chain axis. In this case, E_{dip} (red arrows) are in the *same* direction as the incident field (directed as purple arrows). This means the driving field in

a central NP is *enhanced* by dipolar fields. Note, while E_{pol}(green arrow) is opposite to the incident field, and causes some weakening, I will show quantitatively in Chapter 2 that this damping is dominated by dipole field enhancement. Enhancement means a larger driving force acting on free electrons in a NP, which leads to larger SPR frequency. And, larger frequency corresponds to a blue-shifted collective SPR band with respect to an individual SPR wavelength. In summary, for p-polarized light the collective SPR is longer than SPR wavelength of an individual NP.

Why is this picture different dor large distances between particles? As I already mentioned, increase of the distance between the particles leads to retardation effects: dipolar fields are retarded with respect to the incident field. This results in opposite behavior for the collective SPR mode: p-polarized SPR band shifts into the blue spectrum and s-polarized SPR band shifts into the red. [25]

Let me now summarize a potential application of these SPR-shifts in a molecular ruler. First, the theoretical calculations of the resonance wavelength are carried out. Second, the experimental polarization mapping of the sample is performed: extinction (or scattering, Figure 1) spectra are recorded for different polarization of the incident light. Finally, NPs chain orientation and inter-particle distance are determined based on comparison of the theory and experiment. The more accurate are theoretical calculations, the lower is the error of the molecular ruler.

Two main issues with common knowledge about molecular rulers are: (1) lack of a fine experimental polarization map, which would include broad range of inter-particle distances (I address this issue by presenting experimental extinction map with (1-12) inter-particle distance/diameter range, and (0^o – 180^o) polarization range); and (2) a luck

of a corresponding theoretical map, which would be in a good agreement with the experiment, and would not include any fitting parameters. In general, theoretical background is available from many sources, however it uses varying simplifications, assumptions, and fitting parameters. [23,26] Experimental justification for these simplifications is rather sparse. [15,18,27,28] This raises a question about validity of the theoretical models. I address this issue in Chapter 2 by challenging a *near-field only* assumption, and quantitatively comparing experiment to a theoretical extinction map, calculated without fitting parameters.

Let me explain which simplifications, widely used in literature, I am talking about. In the most general case, the interaction between the nanoparticles in a chain will be determined by *all three* components of the dipolar field: near- $\vec{E}_1$, middle- $\vec{E}_2$, and far-field $\vec{E}_3$. [23]

$$\vec{E}_{dip} = \vec{E}_1 + \vec{E}_2 + \vec{E}_3 = \\ = \frac{1}{4\pi\varepsilon_0}\left(\frac{3\,\vec{n}(\vec{p}\cdot\vec{n}) - \vec{p}}{r^3} - ik\frac{3\,\vec{n}(\vec{p}\cdot\vec{n}) - \vec{p}}{r^2} + k^2\frac{(\vec{n}\times\vec{p})\times\vec{n}}{r}\right)e^{i(\vec{k}\cdot\vec{r}-wt)} \quad (1)$$

where (shown on Figure 3) $\vec{n}$ is the unit-vector of direction of a chain, $\vec{p}$ is the dipole moment induced in a particle, k is wavenumber of a dipole field, and r is the distance between the particles

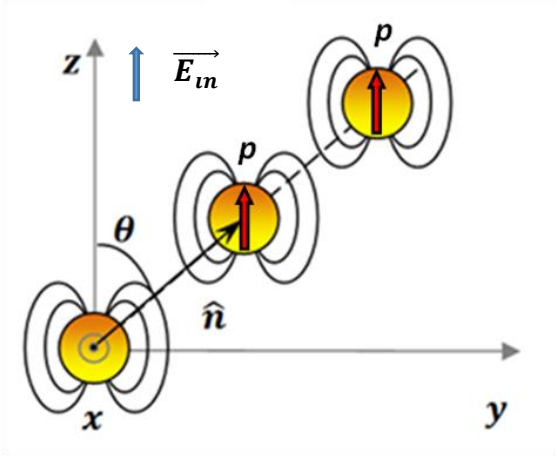

Figure 3. A sketch of a chain of nanoparticles. The incident light is polarized along the z axis. Induced dipoles are represented by red arrows. The chain of nanoparticles is in zy - plane and makes an angle θ in plane of a substrate with the polarization, $\hat{n}$ is a unit vector. Light wave vector is incident along the x-axis. This axis is pointing towards us, out-of-plane. Blue arrow shows incident electric field.

For normal incidence, the angular (angle θ in Figure 3) dependence of the near, middle, and far-fields projected on z-axis is given by:

$$\left(\boldsymbol{E}_1\right)_z = \frac{1}{4\pi\varepsilon_0}\frac{3p\cos^2\theta - p}{d^3}\cos kd \tag{2}$$

$$\left(\boldsymbol{E}_2\right)_z = \frac{1}{4\pi\varepsilon_0}\frac{3p\cos^2\theta - p}{d^3}\left(kd\cos\left(kd - \frac{\pi}{2}\right)\right) \tag{3}$$

$$\left(\boldsymbol{E}_3\right)_z = \frac{1}{4\pi\varepsilon_0}(kd)^2\frac{p\sin^2\theta}{d^3}\cos\left(kd\right) \tag{4}$$

In equations (2) - (4), p is the z-projection of an induced dipole moment in a nanoparticle, k is the wave-vector of the dipole field, d is distance between NPs, and θ is

the angle between chains of NPs and the incident light's polarization vector. Near and middle-field depend on polarization as $cos^2\theta$ and the far-field as $sin^2\theta$.

Previous literature presents the polarization dependence of the SPR wavelength when the angle of the light incidence is varied. [29] However, the polarization dependence of the SPR wavelength *in-plane with the sample* at the normal light incidence has been studied much less. Earlier experiments were performed only for parallel and perpendicular polarizations of the incident light relative to the axis connecting the nanoparticles in the chain. [30,31] There are no reports regarding the whole range of intermediate polarization orientations. The majority of previous reports focused on near-field interactions. [30,32,6,33,34] For example, in [35] neighboring particles with 150 nm diameter and 17 nm height were studied with the distance-to-diameter ratio, *d/D* = [1-3]. Or in [30] nano-rings of 400 nm diameter and 50 nm height were studied with the *d/D* = (1.1 - 1.3). Other studies include [36], where 50 nm diameter and a center-to-center spacing 75, 100 and 125 nm were studied (*d/D* = (1.5 – 2.5)), as well as [32], where 150 nm spherical particles in the *d/D* = [1 – 1.5] range were investigated. [14,33,34] All sources, mentioned above, study samples with small *d/D*, but what about higher *d/D*?

Only a few focused on the far-field. Lamprecht et al. [28] experimentally studied far-field interactions in 2D arrays of flat (14 nm height and 150 nm in diameter) particles and found agreement with a theory presented by Meier et al. [37] It is, however, important to study the whole range of interactions for applications such as the molecular ruler and wave guiding.

It is also important to know at which distances between the particles the dominate interaction changes from the near- to the far-field. The in-plane polarization dependence

of the SPR wavelength is an indicator of this transition. No experimental results have been reported on simultaneous in-plane polarization and distance dependence of collective SPR in a chain of nanoparticles. In Chapter 2, the range of distances between nanoparticles, for which the polarization dependence was studied, spans over the entire range of interactions from near to far-field, d/D = [1 – 12.4]. The angle between polarization and chain of particles is varied in 10^o increments. Finally, this chapter also presents a simple model for (1D) chains of spherical nanoparticles, where the interaction between chains is negligible. Previous reports either study 2D arrays, [29,38] or non-spherical nanoparticles (L-shaped, [38] rectangles, [31] rings, [30] discs, [6] ellipsoids, [33] and hollow spheres). [34]

As I show in Section 2.3, near-field only assumptions do not provide quantitative experiment-theory match for 50 nm NPs even for d/D = 1. The percent difference introduced by this assumption is 5%, which is unacceptable for this effect, since collective SPR shifts with respect to individual SPR are only 26 nm, which is on the order of 5% of the individual SPR wavelength (530 nm). In other words, the wavelength shift can not be distinquished from the error, because both of them are equal to 5%. Neither does far-field assumtoin for d/D = 12 provides good experiment-theory match. I show that for quantitative experiment vs theory match, *all* components of the dipole field (near-, middle-, and far-) must be used.

Let's now consider a fundamental question "for which distance d^* between NPs does near- and middle-field interactions *transition* into far-field interaction?" Even better would be to find for which d^*/D ratio does this transition happen. Experimentally such transition can be observed when $\cos^2\theta$ dependence (Equations 2, 3) transitions into

$\sin^2\theta$ dependence (Equation 4). In other words, we are interested in *d/D,* for which SPR wavelength is θ- independent, or polarization-independent. In our experiment this transition happened for *d/D* = 6.2 (Section 2.4)

There is a fundamental disagreement in literature regarding the transition distance *d**. As a reference, some authors suggested to use a ratio between d^*/D , [27,39,35] or, alternatively, the ratio between d^* and the wavelength. [40,41,36] The situation becomes even more complicated if one recalls the classical electrodynamics definition of the near- and far-field zones of the radiation. [23] The coupling between the particles at the distances $d \geq \lambda/6$ many authors define as the far-field coupling, although from the point of view of the classical electrodynamics this should be defined as the near-field coupling.

Confusion also arises regarding the precise and correct description of the coupling between the particles at the distances comparable with the wavelength of the electromagnetic radiation. Most of the times, the size of nanoparticles is much smaller than the wavelength of the incident electromagnetic radiation (like it is in our experiment), and thus the particles can be considered as point dipoles induced by the incident electromagnetic wave. The electromagnetic coupling between the particles is mediated by the dipole field, in which the middle-field term contributes significantly to the total dipole field at the distance $d \sim \lambda$. However, this contribution has not been taken into account so far. All the publications devoted to electromagnetic interaction between the particles in arrays have not considered the contribution from middle- field. To address the issues described above, I calculate resonance SPR wavelength, explicitly taking into account each component of the dipole field, and then compare results with the experimental resonance wavelength.

1.3 Motivation for the study of silver nanoparticle colloids

Silver NPs exhibit the strongest SPR, compared to other noble metals. While in the previous section I discussed why the SPR wavelength depends on the interactions between NPs, I did not mention that it depends on the particle's size, because all particles in that study were of the same size. In fact, wavelength of a surface plasmon is strongly dependent on a particle's size: as NP diameter increases, the SPR wavelength shifts to the red part of the spectrum. [9] It is a well-known phenomenon and can be intuitively explained by confinement of a SP mode by the boundaries of a particle: the larger the particle, the longer the wavelength of a SP wave must be, analogically to fundamental modes in a resonator cavity. While the size-dependence of SPR in extinction (absorbance and scattering) spectra is well-known, the size-dependent photoluminescence has been studied much less, despite its potential applications in solar cells, [7] surface enhanced Raman scattering (SERS), [42] and bio-imaging. [43,44] "How and why photoluminescence depends on a particle size?" is the question at the heart of a Chapter 3. Answering this question provides additional understanding of the mechanism of emission, and tunability for bio-imaging applications.

The mechanism of an intrinsic photoluminescence of metal nanoparticles is still causing arguments in the scientific community. [45,44,46] Quantum effects, related to size confinement (reasonable for particles smaller than 5 nm, and polycrystalline NPs with the domain size ~ 2 nm), [47,48] radiative damping of SPR (also called plasmon emission), [45] and interband transitions enhanced by local field due to SPs, [49,50] are the most widely used models for description of a metal particle's photoluminescence (PL). Let's briefly discuss each of the mechanisms.

First mechanism: PL due to the *quantum-size effects* is widely applied for rationalization of PL in semiconductor NPs, also called *quantum dots* (QD). The name originates from the similarity of optical properties of QDs to a quantum mechanical particle in a box. Absorption of light results in the creation of an electron–hole pair. Recombination of the pair can result in emission. Size-dependence of PL is related to modification of the energy band gap in these particles, due to the size confinement: the smaller the size of a semiconductor quantum dot, the larger is the energy band gap. [51] Photons, emitted during *e-h* recombination through a large band gap, have large frequency, and hence PL wavelength is small. In summary, the smaller the particle, the shorter the wavelength of PL. Such size effect in PL has been observed for noble metal NPs as well, however NPs are of a very small size (few atoms) (Figure 4). [47,48] Figure 4 (b) represents schematic energy levels diagram for single silver atom, few atom cluster, and a nanoparticle. Absence of electron transitions through a band gap in larger metal NPs is explained simply by absence of a band gap in metals. However, as size of a particle decreases, number of free electrons in a particle becomes too small to create continuous bands, and a band gap appears.

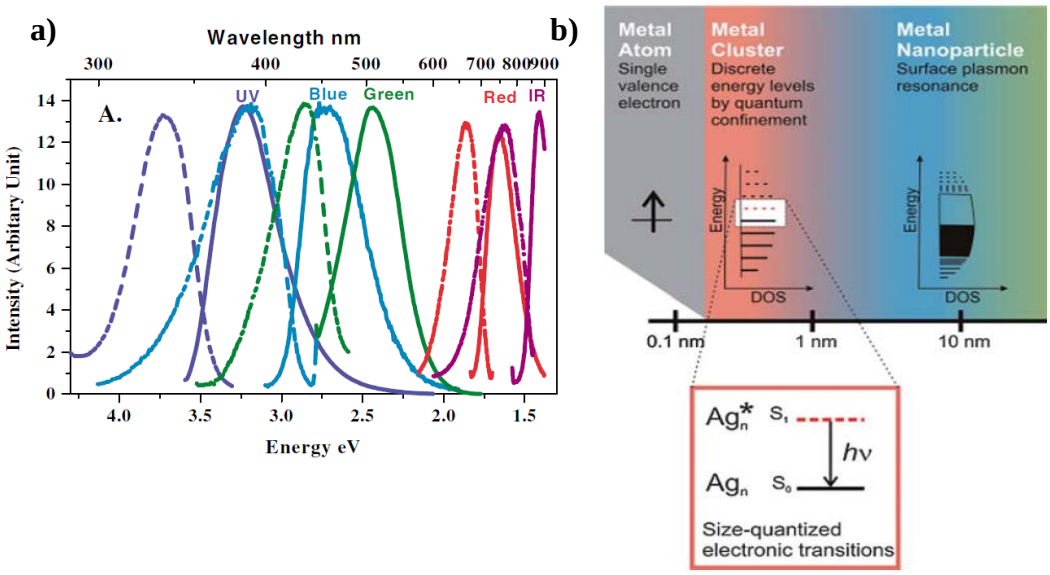

Figure 4 a) Excitation (dashed) and emission (solid) spectra of different gold nanoclusters. Emission from the longest wavelength sample was limited by the detector response. A purple curve – Au_5, blue – Au_8, green – Au_{13}, red – Au_{23}, magenta – Au_{31}. Reused from Ref. [52] with permission from The American Physical Society. b) Adapted from Ref. [53] with permission from The Royal Society of Chemistry.

As one can see from Figure 4 (a), PL emission and excitation extremely sensitive to the particle's size. Related mechanism of PL has also been proposed for multi-domain NPs. [46] Examples of such particles are presented on Figure 5. The PL was reported from poly-crystalline particles with average domain size 1 - 2 nm, while particles with average 8 nm domain (Figure 5 (a)) size were non-luminescent. No size-dependence of the PL was reported for such NPs.

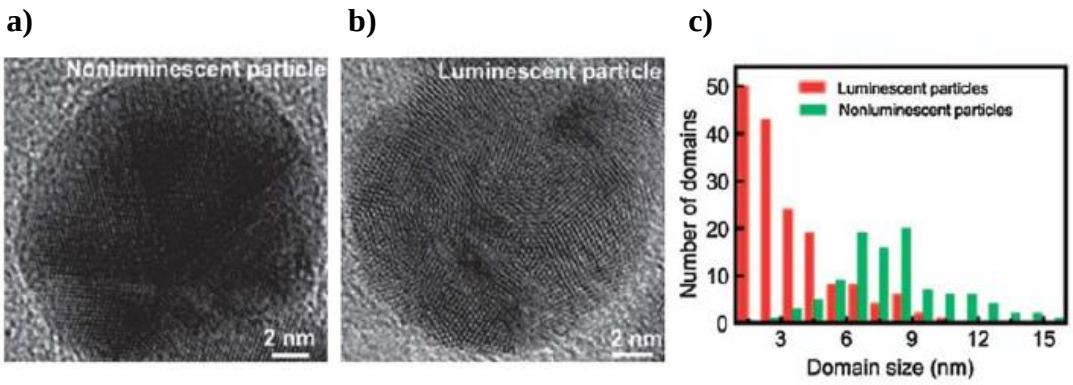

Figure 5. Structural characterizations of silver NPs by HRTEM. TEM images of a nonluminescent NP created by solution-phase synthesis (a) and a luminescent NP created by solid-phase synthesis (b). (c) Domain size distributions obtained from luminescent (red) and nonluminescent (green) NPs. In each case, 15 NPs were characterized. Domain sizes were measured as the average of the long and short axes of the individual domains. Adapted with permission from (LUMINESCENT AND RAMAN ACTIVE SILVER NANOPARTICLES WITH POLYCRYSTALLINE STRUCTURE, J. AM. CHEM. SOC., 2008, 130 (32), PP 10472–10473). Copyright (2008) American Chemical Society.

Future study of our samples could shed light into domain size in our NPs, and potentially explain some of the PL signal using this mechanism. At this point we have preliminary results from a few NPs study with high resolution transmission electron microscopy (HRTEM). These results confirm poly-crystallinity of our samples, but the domain size is > 10 nm (Figure 6 (a)). A more comprehensive study with a large number of NPs could provide additional data and answer the question “do some of the particles have domains of ~ 2 nm, and are they fluorescent?”.

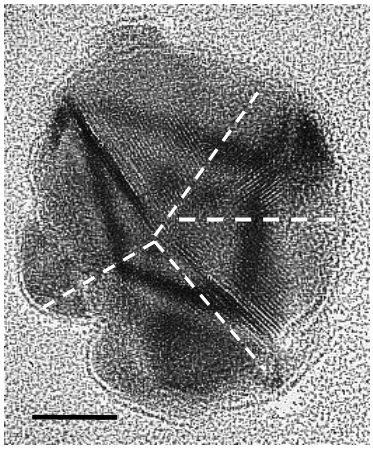

Figure 6. HRTEM of one of our glycine-dimer-coated silver NPs. Scale bar corresponds to 10 nm. Multiple, relatively large, domains are distinguishable within the NP.

Second mechanism: PL due to the *radiative damping of SPR (also called plasmon emission)* is a 3-step process (Figure 7), in which a photoexcited *d*-band hole relaxes within the *d* band, then scatters to the conduction band via emission of a plasmon, which subsequently decays radiatively. More detailed description of this mechanism can be found in the article by Dulkeith et. al [45]. Figure 7 presents a schematic of mentioned 3-step process, adapted from this article. Here PP is a particle plasmon, which is the same as a surface plasmon in a NP. The so-called L-point is the onset point of interband transitions between the *5d* and *6sp* bands in silver. [9]

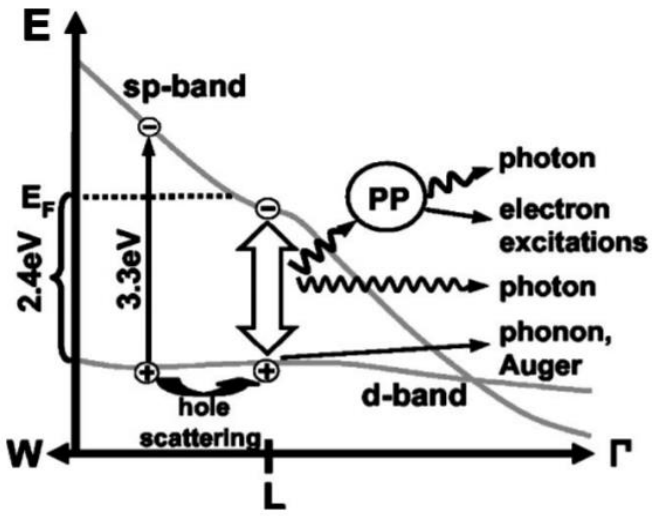

Figure 7. Schematic representation of d → sp interband excitation and subsequent hole relaxation close to the L point of the band structure of gold. A photon with 3.3 eV energy promotes electrons from the d band into the sp band well above the Fermi level. The holes in the d band undergo Auger scattering and hole-phonon scattering. Direct radiative recombination of a d-band hole with an electron in the sp band below the Fermi surface or emission of a particle plasmon (PP) may occur. The PP subsequently decays either radiatively or non-radiatively. Reused from Ref. *[45]* with permission from The American Physical Society.

Third mechanism: PL due to the *interband transitions enhanced by local field due to SPs* is a 2-step process in which electrons from *sp*-band recombine radiatively with the holes in *d*-band. Since there is no band gap between *d*- and *sp*- bands, this process has very low probability. In bulk metals this is primary mechanism of PL, which explains why most of us have never heard of PL from a bulk metal. [54] In NPs surface plasmons create strong local field which can enhance interband PL. [49]

PL in the last two mechanisms, can be excited only with UV light (near the interband edge). On the other hand, PL due to the *quantum size effect* can be excited with lower energy photons (in the visible range). This allows to easily eliminate the quantum size effect mechanism, since for excitation in the visible range no size-dependent

emission was observed in our experiments. It is also an expected result, since mean size of our NPs is greater than 10 nm.

One can distinguish between the two remaining mechanisms (radiative plasmon decay and interband transitions) via testing experimentally size-dependence of the emission. Only in the radiative plasmon decay mechanism the spectral PL emission peak would depend on a particle's size. [45] Figure 8 shows an example of PL, rationalized as radiative plasmon decay: inset shows that spectral peak position on extinction (same as optical density) and PL both shift to the lower energy, as the size of a particle increases. This finding is consistent with our results. Particularly, in Chapter 3 I show that the spectral peak of emission shifts to the red part of the spectrum as NPs size increases. Same is true for the optical density.

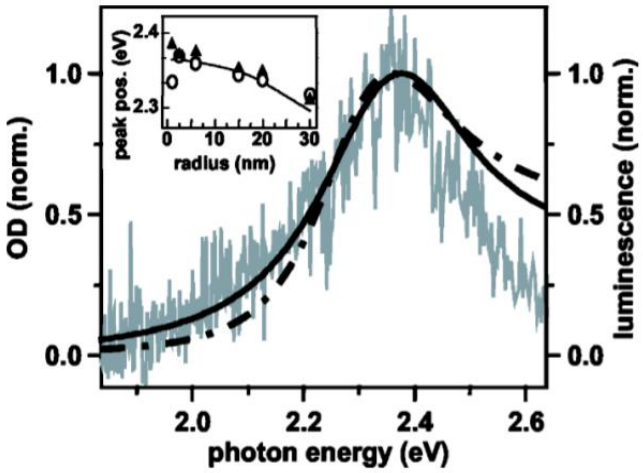

Figure 8. a) Optical density (OD, black line) and photoluminescence (PL, grey line) spectra from gold nanoparticles of 6 nm radius. The dashed-dotted line shows an extinction spectrum calculated using Mie theory. The peak positions of all spectra coincide, indicating the plasmonic nature of the PL. The inset shows the peak positions of OD (triangles) and PL (open circles) spectra from gold nanoparticle solutions of different radii. The solid line represents maxima calculated using Mie theory. The peak positions of the PL closely follow the particle plasmon resonance position. Reused from Ref. [45] with permission from The American Physical Society.

Because of variety of proposed mechanisms for NP's luminescence, it is important to study size dependence of PL, to contribute to better understanding of the NP's PL phenomenon.

A separate interesting question is emission, which originates from the fluorescent molecules on a metal surface. NPs surface plasmons create strong local electric field on their surface, and it enhances PL of the fluorescent labels, attached to a NP. One of recent works (Figure 8) suggesting up to 10-fold fluorescence enhancement.

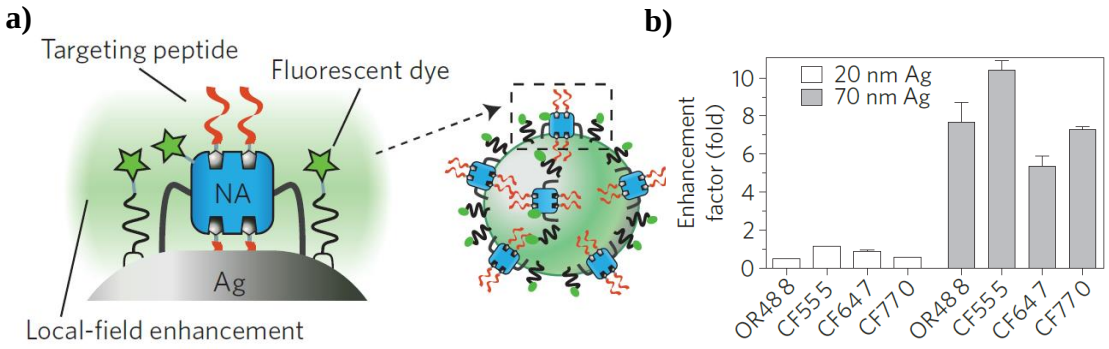

Figure 9. a) Schematic of Ag NPs coated with NeutrAvidin-PEG-thiol (NA) and lipoic-PEG-amine (black lines), onto which fluorescent dyes (stars) are attached, the brightness of the dyes is enhanced by the local plasmonic field. Plasmonic enhancement is lost for etched particles. b) Enhancement factors for several commonly used dyes show a strong dependence on the size of the Ag particle core. Enhancement factors were calculated from the ratio of fluorescence for unetched and etched Ag–NA-dye conjugates. On the x axis is the name of each dye with its approximate peak absorption wavelength in nm. Error bars are standard deviations from replicate wells. OR488, Oregon Green 488; CF dyes from Biotium. Reprinted by permission from Macmillan Publishers Ltd: [NATURE MATERIALS] [55], copyright (2014)

Joseph Lakowicz and co-authors also studied the interactions of fluorophores with metallic particles. [56] In one of their works they found 30-fold increase in the intensity of indocyanine green ICG (dye widely used for in vivo medical testing), which was held close to the silver NP surface by adsorbed albumin. [57] The PL enhancement depends on NP size, and on the overlap of NP's SPR spectral range with the excitation

and emission spectral ranges of the fluorescent molecule. The better the overlap, the higher the quantum yield of a molecule-particle system. [58]

In samples, presented in Section 3.5, PL emission originates from a glycine dimer on a particle's surface, and it's quantum yield depends on the particle's size. We rationalize this dependence by size-dependence of the SPR enhancement. [58,59] In Chapter 3 I show experimentally size-dependence of a quantum yield of a molecule-particle system to be non-monotonic. In addition, to our best knowledge, this is the first-time synthesis of fluorescent glycine dimers during a silver NP synthesis, and study of the mechanism of their fluorescence enhancement has been reported.

In Chapter 3 I also show that our NP-ligand systems are useful for bio-imaging of rat basophilic leukemia and neural stem cells, non-toxic up to 10 micro-molar silver atom concentration, and rapidly etchable (removable from the cell). While use of fluorescent-labeled metal NPs for drug delivery, therapeutics, diagnostics, sensing is very promising, removing particles after they accomplished their mission is an important issue. Dye-labelled polymers, iron oxide, quantum dots, and gold NPs have been extensively studied, however, their removal requires harsh conditions which limit utility (for example, dimethylformamide, strong acid, or iodine). [55] Etchant solution, used is bio-compatible and has been shown not to interfere with the cell's physiology. [55]

A related issue, namely distinguishing internalized NPs from cell surface-bound particles, often is not addressed in the literature. [60] This causes uncertainties in quantitative evaluation of number of particles internalized within the cell, and hinders the cell-particle interaction mechanisms. In Chapter 3 I present dynamics of NP's etching in different solutions, as well as cell-surface-bound NPs.

1.4 Motivation for the study of thin gold films of different morphology

Let's now move from the SP in particles to SP in thin metal films. Nano-films are widely used in bio-chemical sensing. [19] Sensors based on the attenuated total internal reflection (ATR) use extreme sensitivity of the SP to the environment adjacent to the metal film. Commercial sensors have been available from Biacore since 1990s. A key issue in bio-sensing based on thin gold films is the quality and optical properties of the metallic film. This issue I will discuss in Chapter 4. For example, a recent paper [61] has emphasized that the optical properties of the metallic film must be determined by multiple techniques (transmittance and ellipsometry) and through a self-consistent method. Multiple techniques are required because theoretical treatment of a film is not unique: different combinations of fitting parameters can fit an experiment, while there should be a unique set of theoretical parameters (like unique fill-factor and film thickness), corresponding to a unique quality of a film. For example, for gold films with rough surfaces, effective medium theory [8] may be used to model the average of gold and air areas on a rough surface. A question we attempted to answer in Chapter 4 was "is it always possible to obtain a sensible effective medium description of the metallic film, particularly for thin films with rough surfaces?" A solution proposed is to use theoretical parameters, which would allow to match results obtained from few experimental techniques *simultaneously*. The techniques I use are optical transmittance, ATR and atomic force microscopy.

SP in films are different from SP in NPs, introduced earlier, because they are propagating along the metal-dielectric interface. They are also harder to excite: special excitation geometry is needed in experimental study. The SP modes, propagating along

the film surface, are called *surface plasmon polaritons* (SPP). Electric and magnetic fields exists in both, the metal and dielectric, but its' strength falls exponentially as the distance from the interface increases. The condition for SPP excitation at such an interface is found in the matching of an incident photon momentum with a surface plasmon momentum, as well as their frequencies:

$$(k_{SP})_x{}^2 = k_p{}^2 \frac{\varepsilon_m/\varepsilon_d}{\varepsilon_m/\varepsilon_d + 1} \tag{5}$$

This equation describes dispersion for SP. Derivation can be found in works by Guntzer, 1999, and Raether, 1988.

Because for metals the relative dielectric function is negative in optical range of frequencies, $(\varepsilon_m/\varepsilon_d + 1) > \varepsilon_m/\varepsilon_d$ in Eq.5, and the momentum of a surface plasmon is greater than momentum of an incoming photon, namely,

$$(k_{SP})_x > k_p \tag{6}$$

This means, SP cannot be excited directly with light, unless the momentum of light is increased by passing the light through a medium with higher index of refraction (glass prism for example). The two most famous configurations for SPP excitation are: Otto (1968, excitation comes from the air side), [11] and Kretschmann (1968, excitation from metal side) configuration. [10] In this dissertation, I will consider Kretschmann geometry because it is simpler. Figure 10 illustrates the two geometries. In both configurations, SP on the upper and lower surfaces of a metal film are coupled, because the film thickness (~50 nm) is less than the penetrating depth of surface plasmons.

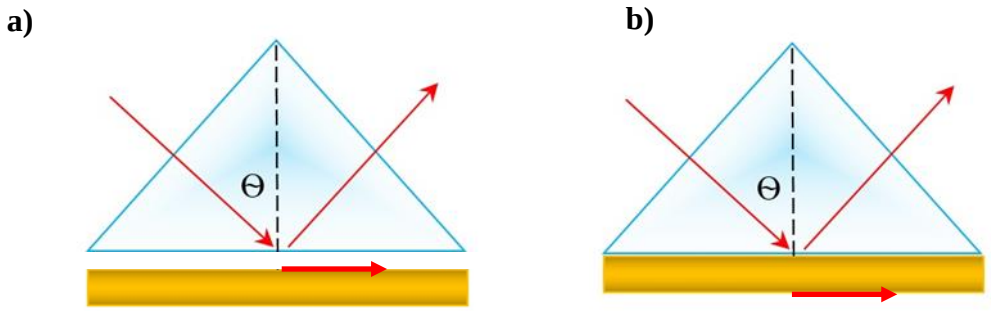

Figure 10. (a) Otto geometry: SP excitation is coming from the air side; (b) Kretschmann geometry: excitation is coming from the metal side. In both cases SP is excited on air-metal interface.

In addition, I present a home-built experimental ATR setup, and it's application for sensing of dynamics of binding events between the gold film and thiol molecules, bovine serum albumin (BSA), and immunoglobulin E (IgE) in Chapter 4.

CHAPTER II

POLARIZATION AND DISTANCE DEPENDENT COUPLING IN LINEAR CHAINS OF GOLD NANOPARTICLES

2.1 Introduction

The focus of this chapter is simultaneous polarization- and distance- dependence of collective SPR wavelength in chains of gold NPs with potential use in molecular rulers, sensors, waveguides, and other applications discussed in the introductory chapter. The main objectives are:

(1) Construct a first-of-a-kind extinction 3D map, where polarization orientation is plotted on the x, inter-particle distance in a chain on the y, and collective SPR wavelength on the z axis: both experimentally and theoretically. The calculations explicitly include the near-, middle-, and far-field dipole coupling between the nanoparticles.

(2) From the match of theory and experiment draw a conclusion about whether near-field or far-field assumptions are feasible for some distances between the particles. I show that experimental SPR wavelength positions are predicted within a 7 nm (1.3%) precision. I interpret this small discrepancy as limitations of the experiment. The theory I used here does not include any fitting parameters in the calculations. With such a match, one can resolve objects separated by distances down to 100 nm with a few nm precision.

(3) From the 3D map, find the inter-particle distance at which the SPR wavelength is polarization-independent, a distance where a transition from near- and middle- to far- field interaction between the particles takes place.

2.2 Experimental results: shift of the resonance wavelength in extinction spectra, dependent on the chain pitch and polarization

Regular arrays of nearly-spherical 50 nm diameter gold nanoparticles were fabricated, using electron beam lithography at Argonne National Laboratory. The area of each array is 2x4 mm and contains linear chains of nanoparticles with a specific pitch, *d.* The chains in the arrays of the nanoparticles are separated by the same distance of 1,000 nm, which provides a high enough density of nanoparticles while still avoiding any electromagnetic coupling between adjacent chains. Figure 11 (a) – (d) shows SEM images of the chains with different pitch, and Figure 11 (e) shows a sketch of the sample.

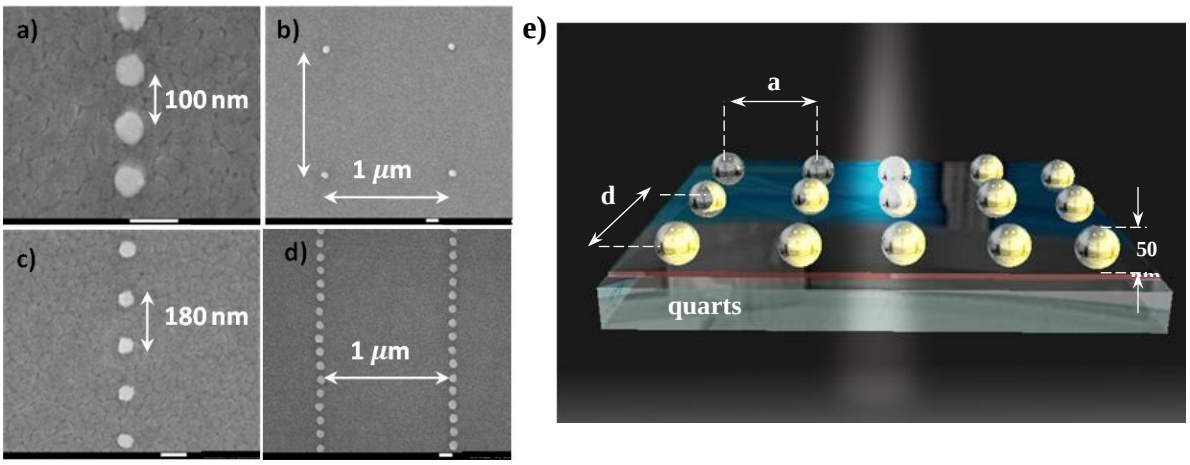

Figure 11. (a) - (d) SEM images of chains with different pitch. Scale bars on all the images correspond to 100 nm. (e) Sketch of the sample.

The optical density of each array was measured using light extinction experiments at normal incidence. Light from a Xenon lamp (denoted as "1" on Figure 12) was collimated (with "2"), linearly polarized (with "3"), and focused onto a 1 mm spot on the array ("4"). The sample was fixed on a rotating platform, and the angle between the sample and the polarization of light was changed from 0^o to 180^o in 10^o increments (inset

(a) on Figure 12 shows rotational stage with the sample on it, and insets on Figure 13 (a) show orientation of the electric field with respect to the chains of nanoparticles). Beam alignment on each array was adjusted with the microscope ("5"). Then, the microscope was removed and transmitted light passed onto fiber optics connected to UV-vis spectrometer ("6").

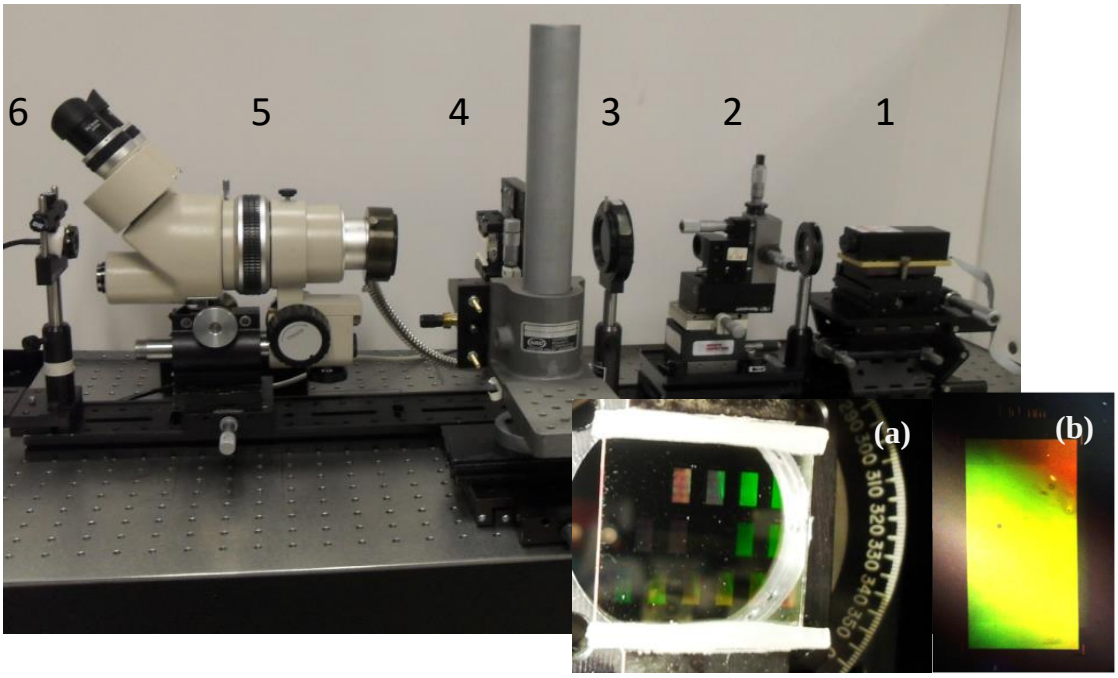

Figure 12. Experimental setup for extinction (optical density) measurements. 1 – light source, 2 – collimator, 3 – polarizer, 4 – sample on rotational stage (enlarged on the inset (a):16 arrays, and (b) a single array), 5 – microscope, 6) spectrometer.

For small distances between nanoparticles (180 nm pitch), the near-field and middle-field electromagnetic coupling is dominant. A red shift in the resonance wavelength is observed as the polarization changed from perpendicular (s-pol) to parallel (p-pol) with respect to the chain (Figure 13 (a)). I qualitatively explain this trend in the introductory chapter. The opposite trend is observed for larger distances between nanoparticles (340 nm, and larger pitches), where the far-field interaction is dominant (Figure 13 (b)).

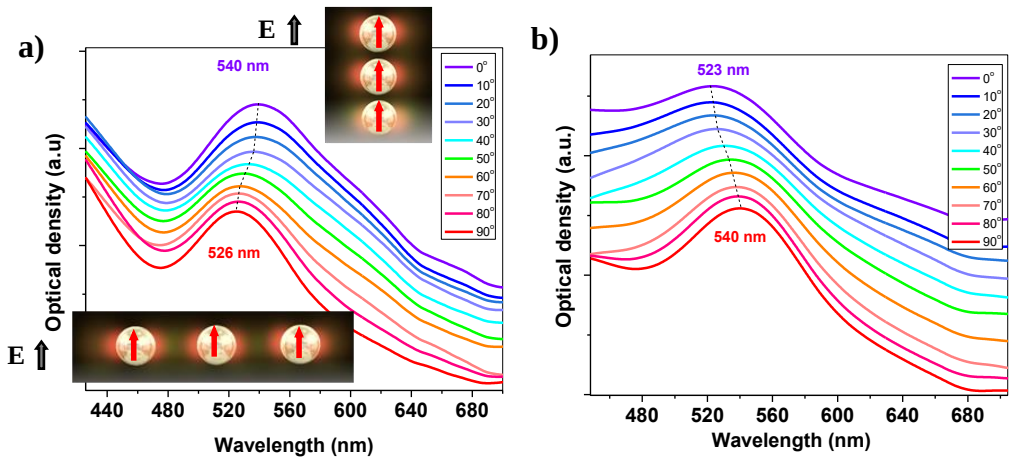

Figure 13. (a) Optical density of an array with 180 nm pitch and (b) 340 nm pitch. Different color curves correspond to different angles between the polarization of the incident light and chains of nanoparticles. SPR wavelength was shifted to the red part of the spectrum for (a) and to the blue part of the spectrum for (b) as polarization changes from s- to p-.

The optical density spectra on Figure 13 were smoothed using the Savitzky-Golay [62] algorithm and then normalized by amplitude via adding a constant in order to illustrate the shift in resonance wavelength. Substrate-only extinction was used as the reference. To confirm that the effect observed here is a result of the inter-chain interactions (1D), a control experiment was performed. I studied a square lattice reference array with a pitch of 1,000 nm. The spectral position of the resonance peak for the reference array is in the 528-530 nm range for all polarization orientations (Figure 14 (b)). This wavelength range is very close to the SPR wavelength of a single 50 nm spherical nanoparticle (533 nm), calculated using the Mie theory. [63] Hence, the interaction between nanoparticles at this distance is very weak and its effects on the resonance wavelength are negligible.

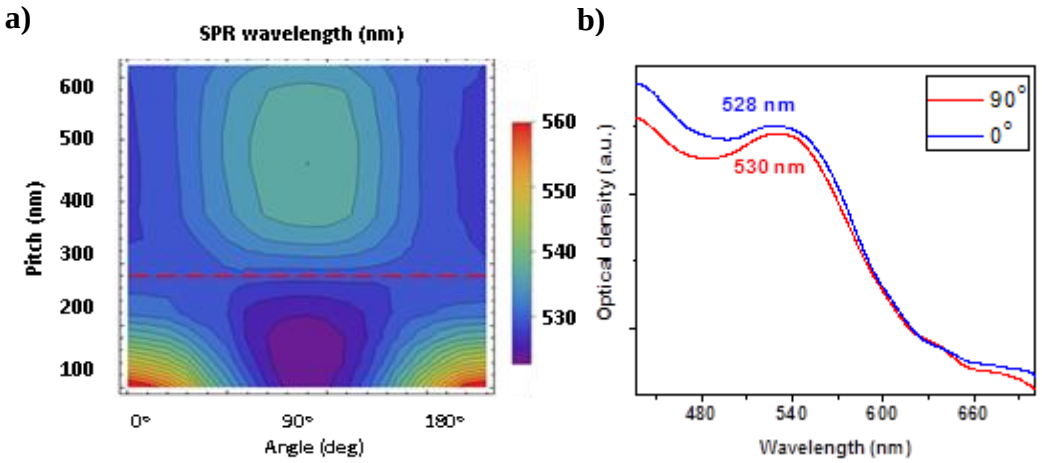

Figure 14 (a) 3D extinction map, obtained experimentally. Red dashed line presents transition pitch, *d**, for which SPR wavelength is polarization-independent. b) optical density (extinction) spectrum of a reference array with SPR peak around 529 nm.

I measured extinction spectra for 16 arrays, with pitch varying from 100 nm to 620 nm, and a control array with 1000 nm pitch. Results for all arrays are summarized in Figure 14 (a). This figure represents the accomplishment of objective (1): experimental 3D extinction map. The next section contains result, which completes the theoretical part of this objective.

First, it can be seen from Figure 14 that the maximum wavelength deviation from single-NP wavelength is observed for the smaller distances between the particles (red and purple areas). This can be explained by the greater density of field lines with small distances between the dipoles. The maxima for Λ_{SPR} corresponded to the parallel polarization of light (0^o and 180^o). As the pitch increases, the maxima are replaced by minima. For the perpendicular polarization (90^o) at short distances, there is a minimum (purple) which is replaced by a maximum for larger pitch (light blue area for 500 nm pitch). Next, the distance between the nanoparticles at which the transition from the near and middle to the far-field is observed as a contour of constant Λ_{SPR} (red dashed line in

Figure 14 (a)). Transition distance, therefore is empirically found to be d^* = 280 nm. This finding accomplished experimental objective (3) for this chapter. I show in the next section that, according to the theory, it should be around 320 nm. This discrepancy most likely comes from the discrete pitches fabricated experimentally, while theoretically pitch could be varied with infinitely small intervals.

2.3 Theoretical prediction of SPR wavelength: assumptions of far-, middle-, and near-field interaction of NPs in a chain

I have introduced far-field $\vec{E}_3$, middle-field $\vec{E}_2$, and near-field $\vec{E}_1$ in Chapter 1. Here I show in details how each of these components of the dipole field affects the SPR wavelength. In the following, I assume that there is no time dependence of the electric field and ignore the e^{-iwt}, and consider the phase difference between the fields $\vec{E}_3$, $\vec{E}_2$, and $\vec{E}_1$. The projection on the z axis, parallel to the incidence of light of the individual component's real parts look like:

$$\left(\vec{E}_1\right)_z = \frac{1}{4\pi\varepsilon_0}\frac{3\,p\,Cos^2\,\theta - p}{d^3}\mathrm{Cos}(kd + \delta_1), \text{ and } e^{i\delta_1} = 1, \delta_1 = 0. \quad (7)$$

where θ is an angle between the unit-vector of a chain and dipole moment induced in a particle, $\vec{p}$, d is distance between the particles (same as r in a previous equation), and δ_1 is phase difference between $\vec{E}_1$ and the incident electric field.

The real part of a complex wave function, representing the middle-field is:

$$\left(\vec{E}_2\right)_z = \frac{kd}{4\pi\varepsilon_0}\frac{3\,p\,Cos^2\,\theta - p}{d^3}\mathrm{Cos}(kd + \delta_2), \text{and } e^{i\delta_2} = -i \quad (8)$$

where δ_2 is phase difference between $\vec{E}_2$ and the incident electric field.

And the real part of a complex wave function, representing the far-field is:

$$\left(\vec{E}_3\right)_z = \frac{k^2 d^2}{4\pi\varepsilon_0}\frac{p\,Sin^2\theta}{d^3}\mathrm{Cos}(kd+\delta_3), \text{and } e^{i\delta_3} = 1 \tag{9}$$

where δ_3 is phase difference between $\vec{E}_3$ and the incident electric field.

The phase of the far-field component is the same as the phase of the near-field component (therefore phase difference $\delta_1 = \delta_3 = 0$), while phase of the middle field component is different (phase difference $\delta_2 = \frac{\pi}{2}$).

Combining z-projections of the real parts of all three fields we obtain total dipolar field, scattered by a particle:

$$\left(\vec{E}_{dip}\right)_z = \left(\vec{E}_1\right)_z + \left(\vec{E}_2\right)_z + \left(\vec{E}_3\right)_z =$$

$$= \frac{1}{4\pi\varepsilon_0}\left[\frac{3\,p\,Cos^2\,\theta - p}{d^3}\left(\mathrm{Cos}\,kd + kd\,\mathrm{Cos}\left(kd - \frac{\pi}{2}\right)\right)\right.$$

$$\left. + (kd)^2\frac{p\,Sin^2\theta}{d^3}\mathrm{Cos}(kd)\right] \tag{10}$$

where I assume that the wave vector $k = \frac{2\pi}{\lambda_{SPR}}$ and λ_{SPR} is the resonance (SPR) wavelength of an individual nanoparticle. In fact, a more accurate wavenumber would be $k = \frac{2\pi}{\Lambda_{SPR}}$, but with this expression, equations can only be solved numerically. This assumption has a negligible effect on the resonance frequency, hence the analytical expression accurately describes the resonance wavelength. A numerically-solved equation led to only a 10^{-2} nm change in Λ_{SPR} in comparison to the analytical solutions.

Using equation (10) the equation of motion of an electron in the polarized NP, projected onto the z-axis for *N*-NPs chain is following:

$$m\frac{d^2z}{dt^2} = -e\left(\vec{E}_{pol} + 2\sum_{n=1}^{N}\left(\vec{E}_{dip}\right)_z\right) \tag{11}$$

where m is the electron mass, e is the electron charge, $\vec{E}_{pol}$ is field created by electron cloud, as a response to the incident electric field, and z is a displacement of a free electron cloud from the neutral equilibrium position relative to the ion core or a particle.

In equation (12) n goes from 1 to N, and $n=1$ corresponds to the nearest neighbors, i.e. the first neighbors close to the NP of the interest. The $n=2$ corresponds to the second nearest neighbors, etc. And the sum of fields is:

$$\sum_{n=1}^{N}\left(\vec{E}_{dip}\right)_n = \left[\left(\vec{E}_1\right)_z + \left(\vec{E}_2\right)_z + \left(\vec{E}_3\right)_z\right]_{n=1} + \left[\left(\vec{E}_1\right)_z + \left(\vec{E}_2\right)_z + \left(\vec{E}_3\right)_z\right]_{n=2} + \cdots \tag{13}$$

Hence, the equation of motion of the electron in the NP in the center of a chain is:

$$m\frac{d^2z}{dt^2} = -e\left(-\frac{p}{3\varepsilon_0 V} + 2\sum_{n=1}^{N}\frac{p}{4\pi\varepsilon_0(nd)^3}\left[(3Cos^2\,\theta - 1) * \right.\right. \\ \left.\left. * \left(\mathrm{Cos}\,knd + knd\,\mathrm{Cos}\left(knd - \frac{\pi}{2}\right)\right) + (knd)^2 Sin^2\theta\,\mathrm{Cos}(knd)\right]\right) \tag{14}$$

Substituting the volume $V = \frac{4}{3}\pi R^3$of a spherical NP of a radius R, and expression for a dipole moment: $p = \mathfrak{N}eVz$, where $\mathfrak{N}$ is number of free electrons, as well as recognizing that plasma frequency squared can be expressed as ${\omega_p}^2 = \frac{ne^2}{3\varepsilon_0 m}$,

$$\frac{d^2z}{dt^2} = {\omega_p}^2 z\left(1 - 2\sum_{n=1}^{N}\frac{R^3}{(nd)^3}\left[(3Cos^2\,\theta - 1) * \right.\right. \\ \left.\left. * \left(\mathrm{Cos}\,knd + knd\,\mathrm{Cos}\left(knd - \frac{\pi}{2}\right)\right) + (knd)^2 Sin^2\theta\,\mathrm{Cos}(knd)\right]\right) \tag{15}$$

where ε_0 is dielectric permittivity of free space, n is number density of free electrons, e is charge of an electron, and m is effective mass of an electron. A ratio of frequency of the plasma oscillations in a chain of N NPs to the plasma frequency is therefore:

$$\frac{\Omega_{SPR}}{\omega_p} = 1 - 2\sum_{n=1}^{N} \frac{R^3}{(nd)^3}\left[\left(3Cos^2\,\theta(\mathrm{Cos}\,knd - 1) + knd\,\mathrm{Cos}\left(knd - \frac{\pi}{2}\right)\right) + (knd)^2 Sin^2\theta\,\mathrm{Cos}(knd)\right] \quad (16)$$

And, using $\omega = kc = \frac{2\pi}{\lambda}c$ I can write wavelength of the collective mode as:

$$\Lambda_{SPR} = \frac{\lambda_{SPR}}{\sqrt{1 - 2\sum_{n=1}^{N}\frac{R^3}{(nd)^3}\left[(3Cos^2\,\theta - 1)\left(\mathrm{Cos}\,knd + knd\,\mathrm{Cos}\left(knd - \frac{\pi}{2}\right)\right) + (knd)^2 Sin^2\theta\,\mathrm{Cos}(knd)\right]}} \quad (17)$$

where λ_{SPR} is a resonance wavelength of a single spherical NP, θ angle between the polarization of the incident light and axis of the chains of NPs, R is a radius of a NP, d is a pitch of a chain.

Using each field component separately from the equation [18] I calculated the resonance wavelength for pitches 100 nm, 300 nm, and 600 nm (Figure 15) Such pitches were chosen to correspond to our samples, where the shortest inter-particle separation was 100 nm (distance-to-diameter, *d/D* = 2), and the largest pitch was 620 nm (*d/D* = 12.4).

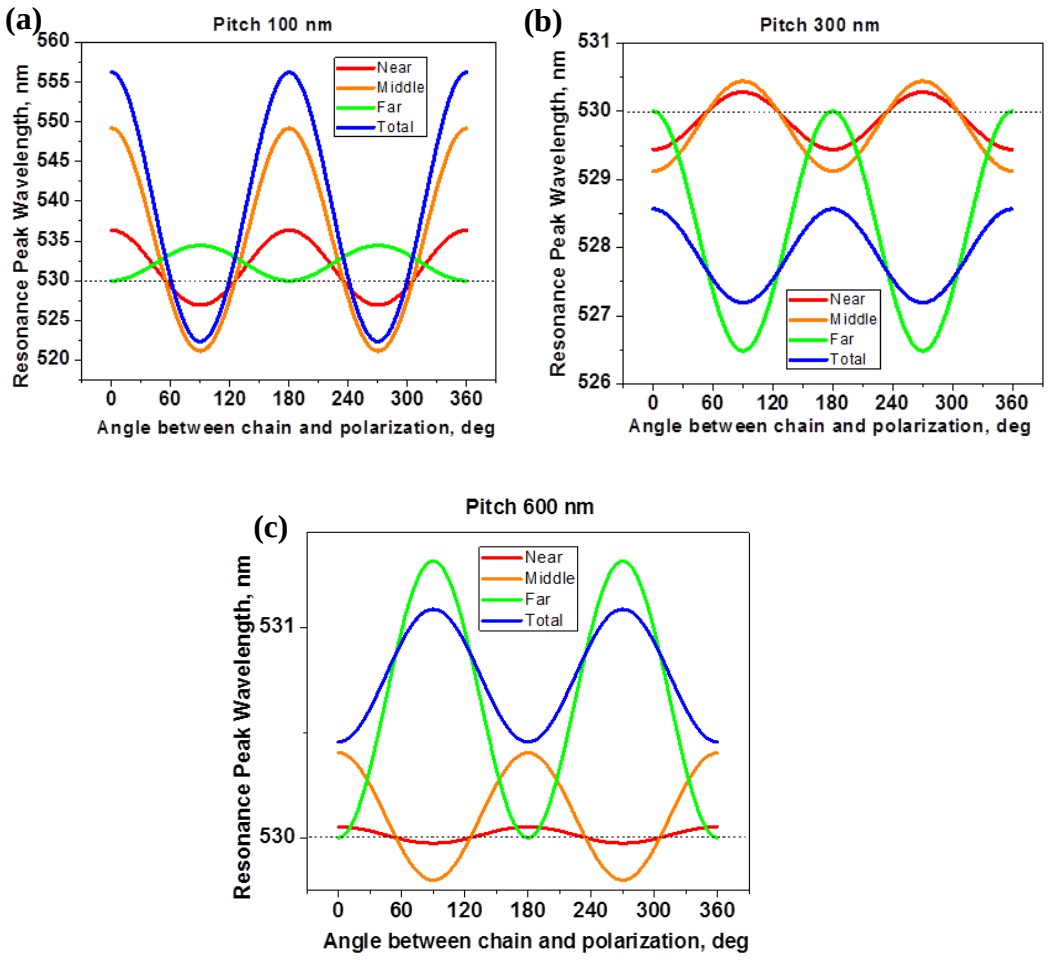

Figure 15. Calculated resonance wavelength of the array with pitch a) 100 nm, b) 300 nm, c) 600 nm as function of polarization orientation. Different colors of curves correspond to contributions of near, middle and far field components.

Figure 15 represents the SPR wavelength dependent on light polarization orientation with respect to the chain of NPs. For 100 nm pitch, which corresponds to distance-to-diameter ratio of 2 (Figure 15 (a)) the middle- field component makes greatest contribution to a resonance wavelength deviations from the single-particle resonance frequency (530 nm). This fact was neglected in some previous studies, and it was generally assumed that only near-field makes the accountable contribution.

[28,35,37] This led to some discrepancies between theory and earlier experimental studies, [35] thus necessitating the use of fitting parameters.

As one can see, the near- and far-field contributions are out-of-phase, so if one were to take into account only these two components, there would be a very slight change in collective resonance wavelength with the change in polarization orientation. In the experiment (Figure 16 (c)) I have observed a strong variation of the resonance wavelength, which advocates for use of the theory, which takes into account the middle-field contribution. The calculated resonance wavelengths are different from the experimental by only 1.3%. Middle field also plays a vital role for larger distances between NPs (Figure 15 (b, c)).

Using resonance SPR wavelengths, calculated as described above for $d/D = [1 – 12.4]$, I constructed theoretical 3D extinction map, illustrated in Figure 16 (a). I show that at a distance of $d^* = 320$ nm between nanoparticles, the interaction changes from near and middle- field to the far-field. The distance at which the interaction shifts can be viewed as an isotropic point. [26] At this distance, the combined effects of all components of the interacting fields result in the same Λ_{SPR} for all polarizations. This distance (red dashed line in Figure 16) is unique and depends on the dielectric constant of the medium in which nanoparticles are placed. Hence, it can be used for sensing. When the dielectric constant of the medium changes, the iso-point will correspond to some new distance between the nanoparticles.

Comparing experimental and theoretical 3D maps, one can see discrepancy between calculated $d^* = 320$ nm and measured $d^* = 280$ nm (Figure 16(a) vs (b)) This

discrepancy is most likely due to the discrete nature of the experimental data. Experimental pitch was changed every 40 nm, while theoretical pitch was varied by 1 nm.

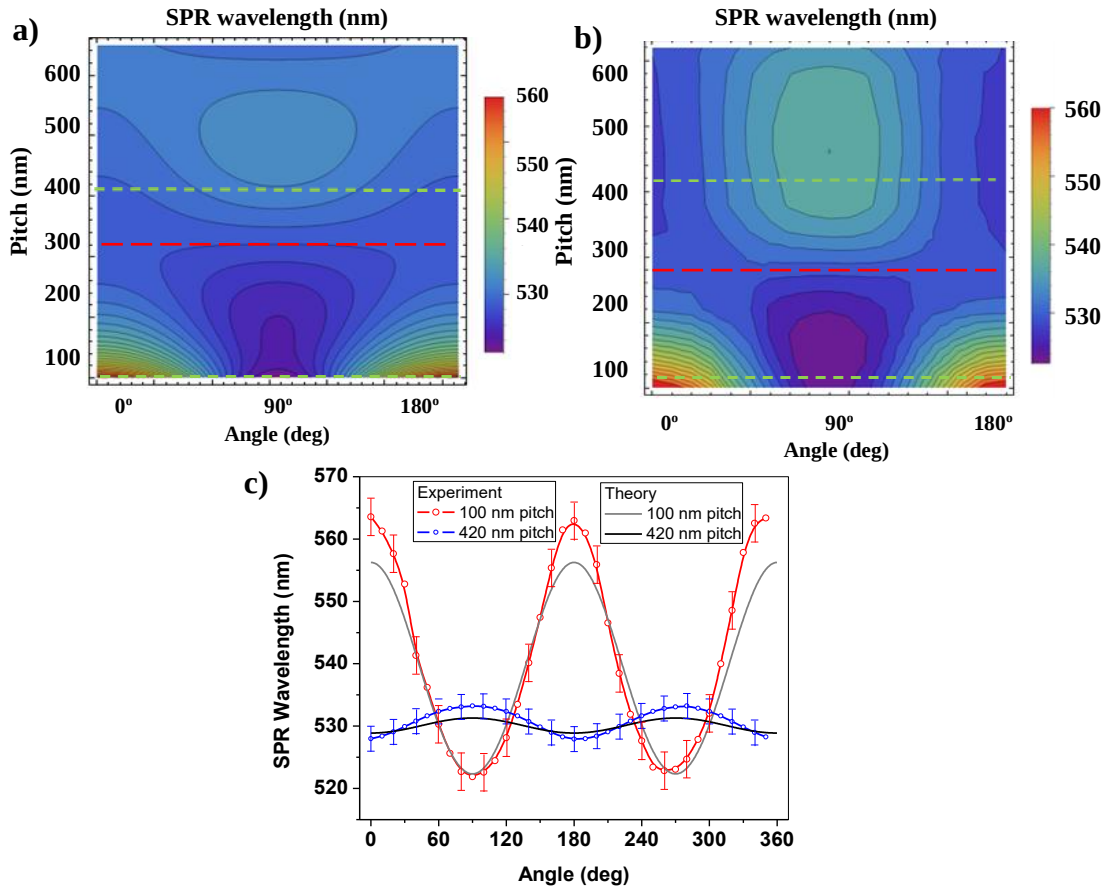

Figure 16 a) Theoretical and b) experimental dependence of the resonance absorption wavelength on the pitch of a chain (y axis) and polarization of the incident light (x-axis). (c) Cross sections of the (a) and (b): Different colors correspond to the arrays with different pitch,100nm - near and 420nm - far-field interaction.

Additionally, the fact that no fitting parameters are included in the theory also leads to some disagreement due to limitations of the equipment (light source instability for example). Future work should include smaller pitch steps in the range around 280 – 320 nm to determine transition distance more precisely. In terms of *d/D*, the transition ratio d^*/D = 5.6 according to the experiment, and 6.4, according to theory.

For better visualization of the data presented in Figure 16 (a, b), I show two cross-sections, denoted by green dashed lines, at the pitch 100 nm and 420 nm. Red and grey curves on Figure 16 (c) represent the SPR wavelength at a 100 nm cross-section from both experiment and theory, respectively. Blue and black curves on Figure 16 (c) represent SPR wavelength at a 420 nm cross-section from both experiment and theory, respectively. Note a near-field-like $cos^2\theta$ dependence for the array with a 100 nm pitch, and a $sin^2\theta$ dependence for the array with a 420 nm pitch, a signature of a far-field interactions.

2.4 Effect of number of particles on the resonance wavelength

Setting the number of particles from 3 to 21 in the equation for most general case of N particles (Equation 17), I found that after the number of particles becomes greater than 20, resonance wavelength approaches a constant. Graphs of the angle-dependent resonance wavelength for 3, 5, 9, 21, and 201 NPs in the chain are shown on Figure 17. Odd numbers of NPs in chain are chosen only because of the general case of infinite chain, fields are usually considered in the central NP (Figure 2). However, calculations may easily be performed for even number of particles, N, slightly modifying the model from 3 particles to 2, and considering dipole field addition from one neighboring particle, instead of 2.

When comparing results for different number of particles in the chain, the greatest deviation of the SPR wavelength corresponds to polarizations parallel (0^o, 180^o) and perpendicular (90^o, 270^o) to the chain. This result agrees with a similar result by Citrin. [64] However in that work the author did not study a broad range of interparticle distance and resonance wavelengths.

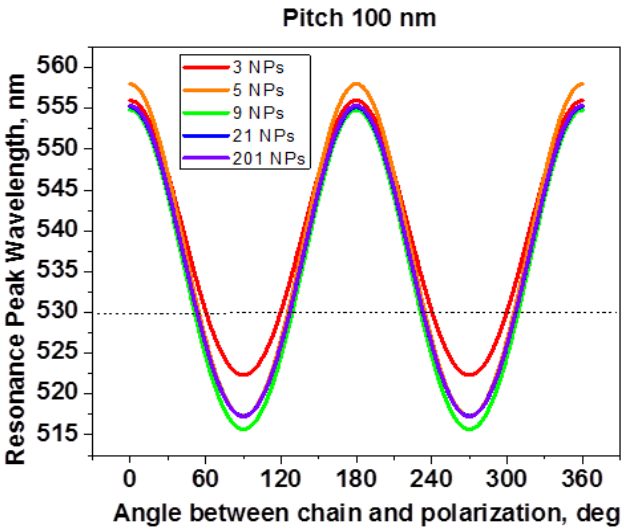

Figure 17. SPR wavelength for a chain of different number of NPs [3, 5, 9, 21, 201] vs the angle between the polarization of the incident light and the axis of the chain. Pitch 100 nm, diameter of all NPs is 50 nm. Dotted horizontal line represents SPR wavelength of an individual 50 nm NP.

Figure 17 shows that as number of NPs in the chain increases, the interaction between them increases as well: deviation of the collective SPR wavelength from single particle SPR (530 nm) becomes greater. However, it is only true up to 21 NPs in the chain. As the number of NPs increases, the wavelength of collective SPR approaches some constant value for a given angle. One can see that for 21 and 201 NPs in the chain SPR wavelength is almost the same.

One may use results from this section for scaling our 3D map for a 3-particle chain, for example, for use in molecular ruler. Future experimental work may include experiments with 2, 3, and up to 200 particles in the chain to test the theoretical prediction described in this section.

2.5 Conclusions

In summary, firs-of-a-kind extinction 3D map was produced both experimentally and theoretically. I show that the peak of the resonance extinction can be tuned by both adjusting the in-plane light polarization and the distance between nanoparticles in the chains. I also show that experimental peak positions for 100 nm pitch is determined to within 7 nm (1.3%) or less of the simulated wavelengths. From the match of theory and experiment I conclude that theoretical calculations of the resonance wavelength must take into account all three components of a dipole field. However qualitatively, one can assume near- and middle- field interactions for $d/D < 6$, approximately, and far-field interactions for $d/D > 6$, as long as diameter D is less than a wavelength of the incident light.

From the 3D extinction map I find the inter-particle distance, where a transition from near- and middle- to far- field interaction between the particles takes place. The $cos^2\theta$ near-field dependence is observed for chain pitches less than 300 nm, while there is a $sin^2\theta$ far-field dependence for larger pitches (340 nm – 620 nm). The transition distance d^*, at which the resonance wavelength is polarization-independent is 280 nm, according to experiment. It is close to the theoretically predicted 320 nm. The discrepancy between the theory and experiment is attributed to the discreetness of the experimental data (particle separation was varied by 40 nm). Coupling becomes negligible when nanoparticles are 1,000 nm apart. Additionally, according to calculations, as number of NPs in the chain approaches 20 the resonance wavelength becomes independent on the particle number.

Results of this chapter are crucial for understanding the distance dependence of nanoparticle collective modes in chains of NP's, and the development of biochemical sensors, [13,6,65,66,67] sub-wavelength wave guiding, [16,68,69] surface enhanced Raman spectroscopy, [70,71] optical tweezing, [5] and enhancement of light absorption by solar cells. [3,72,73] The effects of polarization and number of particles in a chain are especially crucial for molecular ruler applications, [15] where the orientation of the nanoparticles is unknown. Other promising applications of ordered plasmonic nanostructures include use in active thin-film polarizers and filters. [74] Nanoparticle chains in conductive polymers can form a polarizer with tunable efficiency or a filter with a tunable frequency rang.

CHAPTER III

IMAGING OF BIOLOGICAL CELLS USING LUMINESCENT SILVER NANOPARTICLES

3.1 Background

In this chapter, I show how SPR in silver NPs affects their intrinsic PL emission, as well as how it enhances the PL of glycine ligands on the NP's surface. In previous studies, the intrinsic PL of large NPs (diameter > 2 nm, domain size in poly-crystalline NPs > 2 nm) has been rationalized as SPR enhanced interband electronic transitions enhanced by SPR, [44] or alternatively direct plasmon emission due to the radiative damping of the SPR. [45] I explain briefly each of these mechanisms in the introductory chapter. Previous reports have indicated quantum yield (QY) for the intrinsic PL of silver NPs as high as 1.2×10^{-2} for 8 nm NPs, and 4.6×10^{-3} for 11 nm NPs, [44] a somewhat lower quantum yield 10^{-4} - 10^{-5} for 5 nm gold NPs, [75] and even lower 10^{-5} for 17 nm 10^{-6} for bulk copper NPs. [76] All of the mentioned QY values are orders of magnitude larger than that of 10^{-10} for metals. [54]

Another SPR-related effect, the enhancement of a ligand's PL on a nanoparticle's surface, is caused by the strong local field at the NPs surface, whereby the particle enhances the incoming and outgoing photons. The surface enhancement of Raman scattering for Rhodamine 6G was reported to be most efficient for 50 - 60 nm diameter silver NP. [77] According to authors of this study, excitation of SP results in a strong local electromagnetic field enhancement in the vicinity of the nanoparticles. And it is this

local field enhancement that is responsible for the major enhancement in the Raman spectra of molecules near the surface of metal particles. In the experiments presented in this chapter, evidence of the connection between SPR excitations in silver NPs and their intrinsic PL signal is found. This connection is then compared to the surface-enhanced PL of the glycine dimer ligands, with the goal of developing robust, non-toxic, stable and bright fluorescent biomarkers.

3.2 Materials and methods

Materials: All experiments were performed with chemicals and solvents of reagent grade and were used without further modification or purification. For synthetic procedures, glycine (CAS: 56-40-6, Reagent Plus 99%), and silver nitrate (CAS: 7761-88-8, ACS Reagent 99+ %) were purchased from Sigma Aldrich. The quantum yield standard, quinine sulfate (CAS: 207671-44-1, meets USP testing specifications), was purchased from Sigma Aldrich. Aqueous quinine standards were prepared in 0.05 M sulfuric acid ($H2SO4_{(aq)}$, CAS: 7664-93-9, Alfa Aesar). Distilled deionized water (pH 6.3) was used for all experiments and reagent dilutions.

NP's Synthesis: The nanoparticles used for this study were synthesized based on a procedure previously described in the literature. [46] Silver nitrate and glycine (1-to-10 mass ratio) were dissolved in distilled deionized water to form an intimate mixture. The water was then evaporated under low pressure to form a solid crystalline reaction mixture. After solvent evaporation, a solid phase thermal reduction was performed on the crystalline mixture at 445 K for 5 minutes. During this procedure, glycine-dimer-coated silver nanoparticles were formed via a reduction-oxidation reaction, while the solid

glycine matrix controlled the size of these particles. The resulting product was dissolved in water and sonicated for 24 hours to break apart any aggregates. The absorption and emission spectra, obtained every hour during the sonication procedure, showed no evidence of additional product formation (such as nanoclusters). The product was then filtered through a 2 μm pore diameter filter and subjected to a centrifugation procedure that separated the insoluble aggregates and free glycine molecules from the glycine-dimer-coated nanoparticles.

Cell culture: The C17.2 cell line adopted from the cerebellum of newborn mice was supplied by Dr. Evan Y. Snyder from Harvard Medical School, Boston, MA. C17.2 neural stem cells (NSC) were grown in Dulbecco's modified Eagle's medium (DMEM) and supplemented with HEPES, Pen/Strep, L-Glutamine, 10% FBS, and 5% Normal Horse Serum. Rat basophilic leukemia (RBL) cells (RBL-2H3; ATCC number CRL-2256) were maintained in minimal essential medium (MEM) supplemented with 10% fetal bovine serum (FBS), 1% Penicillin Streptomycin (Pen-Strep), and 1% L-glutamine (L-glut).

Centrifugation Procedure: The raw synthetic product had a broad size distribution as was indicated by transmission electron microscopy (TEM) and extinction spectroscopy. In order to study the size dependence of the PL, this raw product was centrifuged to separate the particles by size. Relative centrifugal forces (RCF) of 500g to 14000g were used. As a result, four samples were obtained with different size distributions (Figure 18). The extinction spectra of the NPs separated by size are shown in Figure 19 (b) with the corresponding PL spectra displayed in the Figure 19 (c).

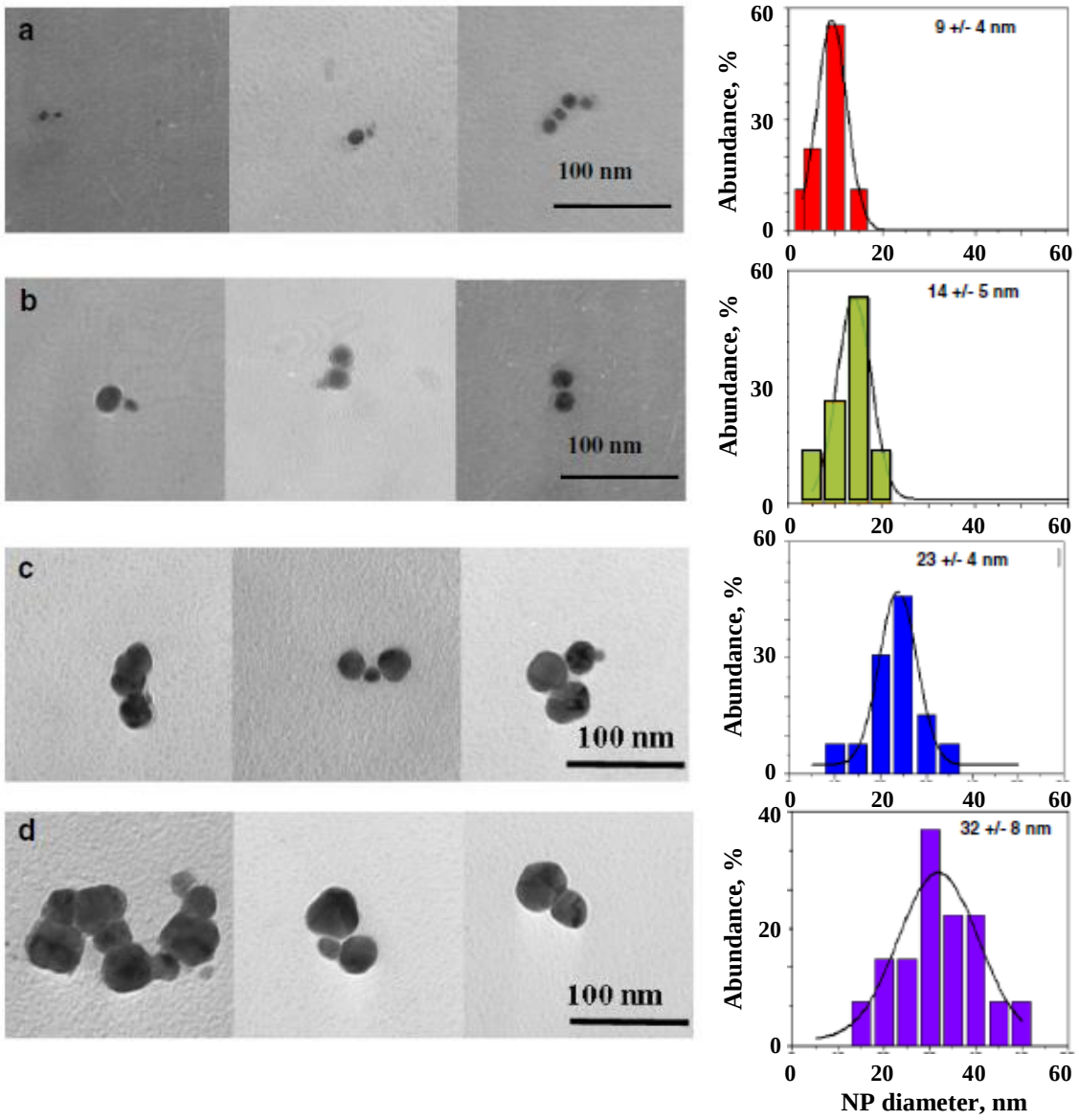

Figure 18. TEM images of silver nanoparticles of different sizes along with their size distributions.

TEM size and shape characterization: Samples containing the desired NPs of different sizes were characterized by a JEOL JEM-100CX electron microscope. Images of selected samples and their size distributions are shown in Figure 18. As was expected,

the largest relative centrifugal force (RCF) applied resulted in the smallest NPs to be found in the supernatant (Figure 18 (a)), and the lowest RCF resulted in the largest NPs to be dragged into a pellet (Figure 18 (d)).

Quantum Yield: Relative QY was determined by comparing the photoluminescence from glycine-dimer coated silver NPs to the well characterized QY standard, Quinine (in 0.05 M $H_2SO_{4\,(aq)}$). Each sample of NPs was matched in its optical density to that of the standard at the excitation wavelength 366 nm (the QY of the quinine is known to be .54 +/- 0.003 when excited at 366 nm). [78] This condition guarantees that the NPs in the sample and the QY standard absorb the same amount of light upon excitation. Once the optical density of the standard and NP samples were matched, the PL spectra were recorded and the relative quantum yields of each sample were calculated using the ratio of the areas under their PL spectra.

Bio-imaging: A Leica TCS SP5 confocal microscope was used to obtain fluorescence and transmission images of neural and RBL cells incubated with NPs. The C17 cells were fixed using 1%, and RBL using 4% paraformaldehyde for 20 min. The paraformaldehyde was then removed, cells were washed with PBS, covered with the media, and imaged with a 40x oil immersion objective. The excitation laser wavelength was 405 nm, and the emission channel was set to 420-535 nm. A 0.2 mL aqueous solution of fluorescent glycine dimer coated NPs, with average diameter 9 +/- 4 nm, were added to the fixed cells, which were contained in 2 mL of media. Imaging was performed every 15 minutes, starting immediately after addition of NPs. Every set of images

included a z-stack of 100 focal planes. Images obtained of cells taken during NP incubation are shown on Figure 23 and Figure 24.

3.3 Intrinsic silver NP photoluminescence

After size separation, the samples contained NPs of mean diameters 9 +/- 4 nm, 14 +/- 5 nm, 23+/-4 nm, and 32+/-8 nm (Figure 18). The smaller particles were near-spherical, while the larger particles were more irregular (compare Figure 18 (a) to Figure 18 (d)).

Optical properties of the particles were then studied to determine their size dependence. The intrinsic silver NP's PL spectra were obtained with the excitation wavelength of 250 nm. This excitation wavelength is within the spectral region of the inter-band absorption for silver (the edge of the interband absorption is at 388 nm). [79] Under a 250 nm excitation the glycine dimer's PL was not excited, and only the size-dependent intrinsic PL of the NPs was observed. It was found that as the NP's diameter increased, the PL peak (Figure 19 (c)) was spectrally shifted towards the red end of the spectrum, like that of the SPR-related peak in absorbance, shown in Figure 19 (b). This shift in absorbance is well-known and has been rationalized by the so-called *polaritonic* effect caused by a phase retardation of the electromagnetic waves (also known as *extrinsic* or *electrodynamic* effect). [9] Multiple experimental studies confirm this effect and have shown a red shift of the SPR peak in the absorbance spectrum as the diameter of the NP increases (for diameters > 10 nm) [12]; however, the same shift in the intrinsic PL has been previously reported in very few studies. [45]

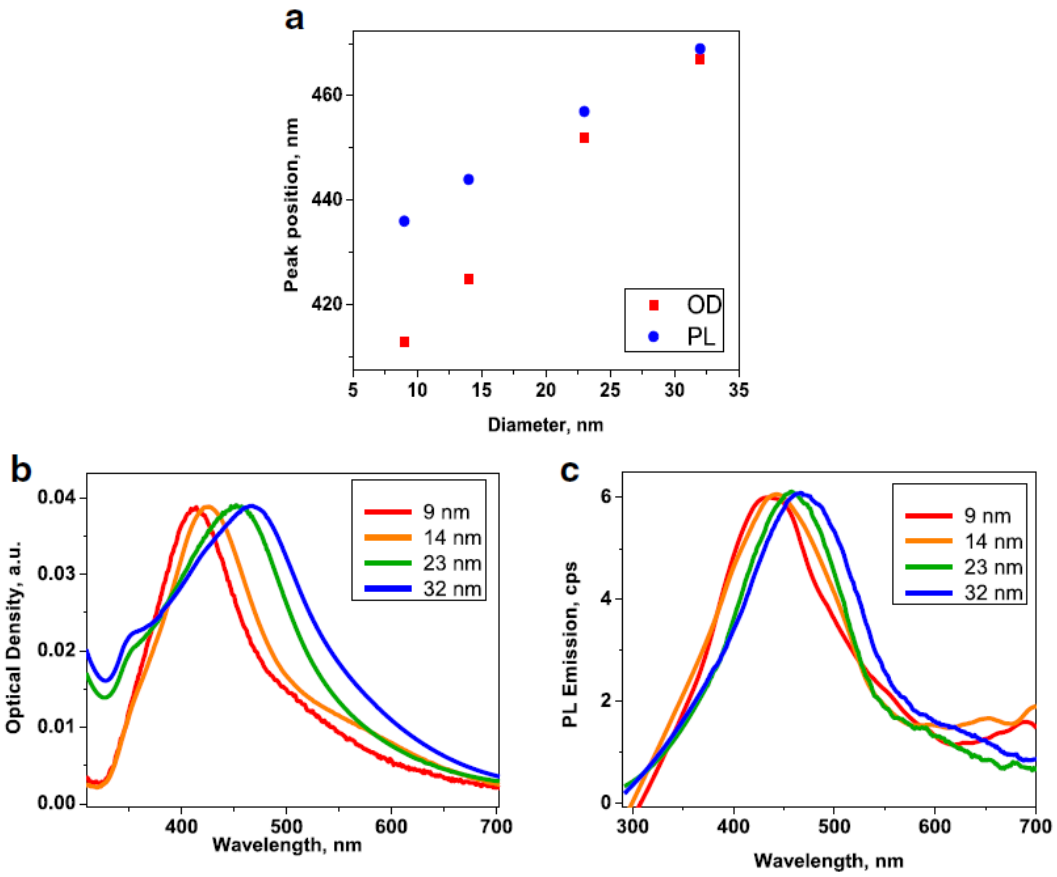

Figure 19. Photoluminescence and extinction spectra of silver nanoparticles in water**.** a) The peak position of PL as the function of NP size. Blue dots correspond to PL emission peak, red dots correspond to optical density (OD). b) Extinction spectra: the OD is a quantitative measure of light extinction (absorbance + scattering). It shows how much light is absorbed and scattered, during light being transmitted (transmittance, T) through the sample. OD and T defined as: $OD = -log(T),\ T = \frac{I_T}{I_0}$, where I_T – intensity of light transmitted, and I_0 -intensity of light entering the sample, c) Photoluminescence emission spectra of nanoparticles of different sizes.

With the observed correlation in position and the shared trend in size-dependence, the spectral shifts of both the PL and absorbance (Optical density, OD) spectra (Figure 19 (a)), indicate that the intrinsic PL of the NPs is due a radiative decay of the SPR. The radiative decay of the SPR in noble metal NPs is also known as plasmon emission, or plasmon scattering because of its very fast (a few femto seconds) decay. [80] It has been

stated that the red shift of both OD and PL spectra is an indicator of the plasmon emission, as opposed to the interband emission mechanism. [45] It is worth noting, that some previous studies have observed PL due to both the interband transitions and plasmon emission in noble metal NPs. [45,44,81]

Comparison of the PL intensity from NPs of different sizes was performed for samples matched in OD at 250 nm. This guaranteed the same number of photons were absorbed by all samples. The intensity of intrinsic PL from the silver NPs increased as their size increased. This is further evidence toward the rationalization of radiation damping as the source of PL in the metal NPs.

Briefly, the mechanism of PL due to a radiative decay was described in the introductory chapter, and is as follows: First, the interband electronic transitions are excited by the incident light. This excitation relaxes into the SPR modes, and the SPR then radiates or emits this energy as photons (radiatively decays). [45] Seen as photoluminescence from the NPs, the energy radiated during this decay process is size-dependent because the SPR is also size-dependent. Evidence for such a PL mechanism in noble metal NPs has been shown in previous studies. [81,82,83]

Despite the low QY observed from the intrinsic PL of metal NPs, much of the recent literature suggests its potential in bio-imaging and other applications. [83] An alternative use of SPR excitations in silver NPs can be found in the enhancement of PL from fluorescent ligands on the surface of a NP. In the next section, the size-dependent surface-enhanced PL of glycine-dimer ligands is reported. Further discussion on how radiative decay affects the surface enhancement of the ligand PL is also provided.

3.4 Surface-enhanced photoluminescence of glycine dimers

During the NP synthesis, glycine forms fluorescent dimers. The dimer formation has been previously reported under conditions different from those in our study, and without the presence of silver nitrate, or silver NPs. [84] To our best knowledge, this study has been the first to demonstrate that fluorescent dimer formation is possible in the presence of silver, and only takes place in a specific temperature range. This temperature range is the same range that produces the greatest yield of NP formation. The FTIR spectra illustrating this effect are shown in Figure 20.

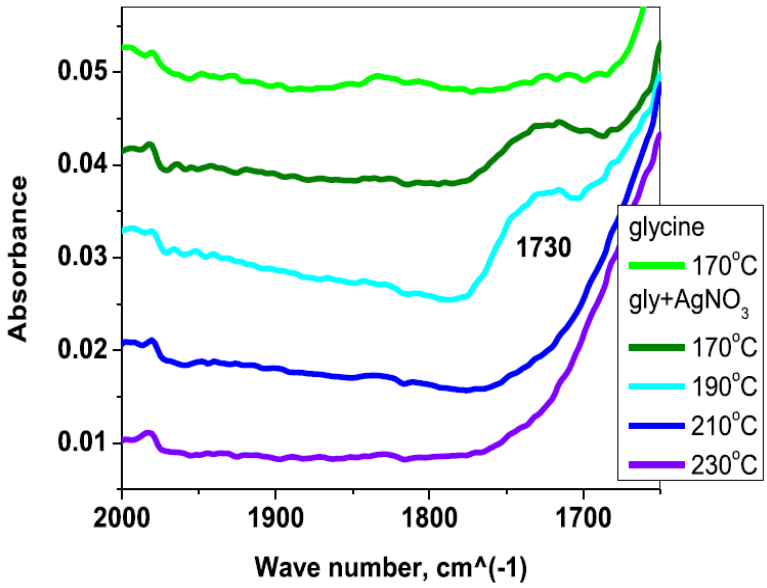

Figure 20. FTIR spectra of mixture of silver nitrate and glycine treated at different temperatures (different colors of the curves). The upper curve (light green) represents pure glycine without silver nitrate.

In Figure 20, the presence of glycine dimers was suggested by the peak around 1730 cm^{-1}, which indicated peptide bond formation, as previously reported. [84] Further proof of the fluorescent glycine dimer formation in our experiments was the NP-glycine-

dimer PL spectra (Figure 21 (a)). They were identical to the spectra of previously reported PL for the cyclic glycine dimers (Figure 21 (b)). [85] The same dependence on the excitation wavelength (Figure 21) as stated in the literature was also found. Glycine was initially chosen as a NP ligand because of the bio-compatibility of this amino acid. The bio-compatibility of the cyclic glycine dimers is yet to be studied.

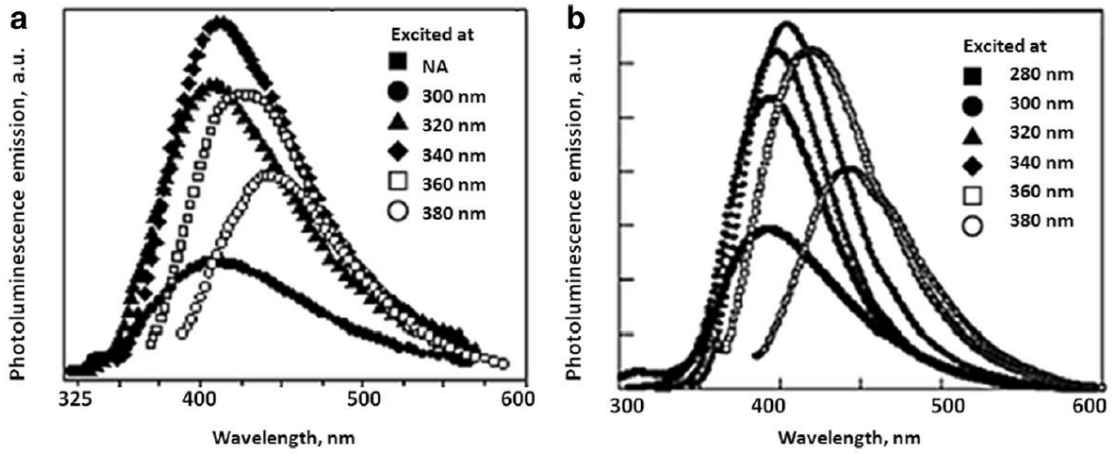

Figure 21. Photoluminescence emission spectra of a) glycine-dimer-NPs of 9 nm average dimeter, b) free-standing glycine dimers. Different curves correspond to different excitation wavelength: squares correspond to 280 nm excitation, circles – 300 nm excitation, triangles – 320 nm, diamonds – 340 nm, empty squares – 360 nm, empty circles – 380 nm. Figure (b) Reprinted from, The Journal of Supercritical Fluids, 41/2, Yasuhiro Futamuraa, Kazuyuki Yaharac, Kenji Yamamotoa, Evidence for the production of fluorescent pyrazine derivatives using supercritical water, Copyright (2007), with permission from Elsevier.

It was found that the quantum yield for the glycine-dimer-NPs was non-monotonically-dependent on the NP's diameter, as it reached a maximum for the 23 nm core diameter NPs. Mainly, for the NP-ligand system, with a mean core diameter of 9 nm the QY was 2.7%, for 23 nm core it was 5.3%, and for 32 nm it was 1.5%. The dimer-NP emission spectral position, however, did not show any noticeable size-dependence (Figure 22), which supports the hypothesis that the origin of this PL is

glycine dimer's emission. In Figure 22 curves have maxima in [425 - 430] nm region, except for the 32 nm sample (purple curve), for which the peak position is skewed due to inset of the excitation peak at 366 nm on the left. The [425 - 430] nm is a negligible size-dependence of PL, compared to the size-dependence of PL excited at 250 nm (Figure 18), where maxima shift is in the [435 – 470] nm range, corresponding to [9 – 32] nm samples.

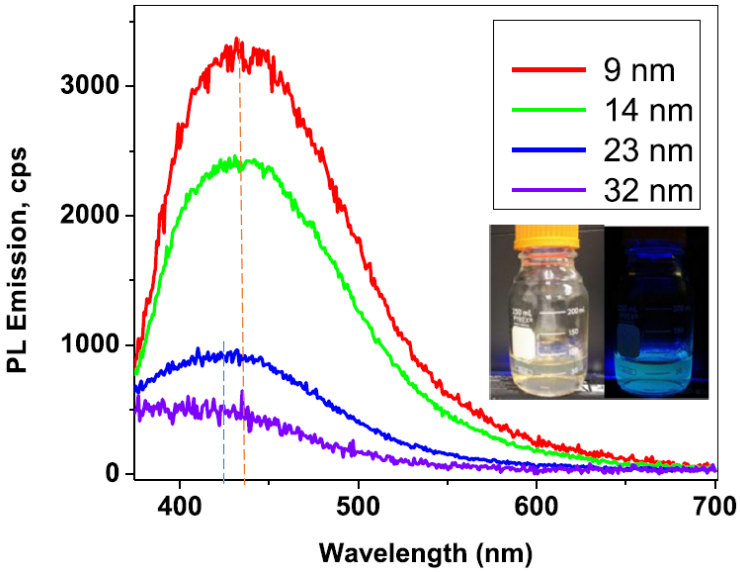

Figure 22. Photoluminescence emission spectra for NPs of different sizes when excited at 366 nm. Different colors of curves correspond to different mean diameters of NPs in the samples. PL emission spectra not adjusted for OD at 366 nm – therefore amplitudes of the spectra are irrelevant. Main idea – negligible size-dependence of spectral position (x-axis) of the PL peaks. Red and blue dashed lines show spectral positions of PL peaks for 9 nm and 23 nm samples. Photographs on the inset show 9 nm diameter NPs in water under day light (left) and UV illuminations (right).

The size dependence of the QY of a dimer-NP system was rationalized by the fact that the local field on the NP's surface is also size-dependent. [44] The local field is dampened via a few mechanisms, including the radiative decay, discussed in a previous

section. The radiative decay increases with the increase of a NP size. [12] This leads to stronger damping of a local field for larger NPs. On the other end of the NP size range, as the diameter of a NP decreases further, the internal size effect dampens the local electric field at its surface. [86] Hence, there exists an optimal size of a NP, for which local field is maximum. This explains experimental observations of maximum PL enhancement of the ligand's emission by NPs of specific diameter.

3.5 Application of labeled silver nanoparticles for imaging of neural stem cells and rat basophilic leukemia cells

To evaluate the possible use of glycine-dimer-NPs as biomarkers fixed neural stem and RBL cells were incubated with NPs. Fluorescence confocal microscopy was then used to study the particles' penetration into the cells.

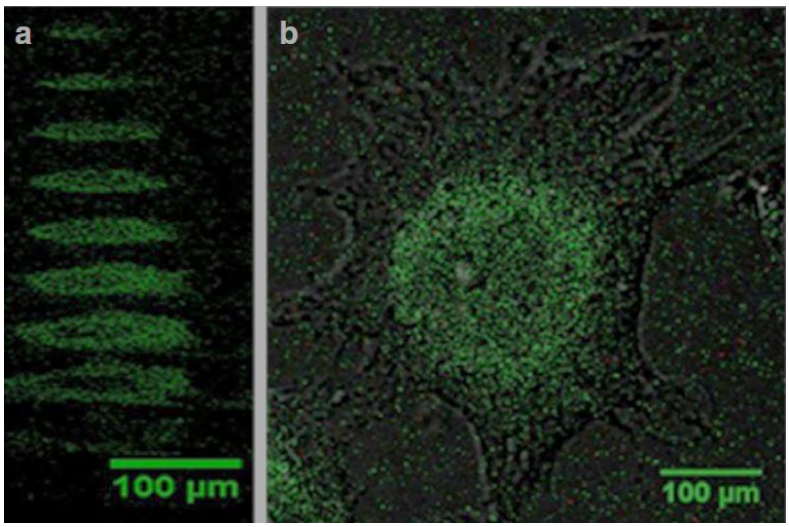

Figure 23. Fluorescent and transmission confocal microscopy image of a neural stem cell. a) Cross-sections (z-stacks) of a cell separated by 1 micrometer, b) top view of a cell as a sum of all z-stacks.

The smallest NPs of 9 nm mean diameter (shown in Figure 18 (a)) were chosen as bio-imaging markers, since small NPs penetrate cell membranes more readily. [87] As one can see in Figure 23 and Figure 24, majority of NPs accumulated on the fixed cells' membrane, while were fewer found in its body (dark area in the center). The fluorescence signal seen in the background of Figure 23, was most likely caused by the presence of residual particles in the cell media. Images in Figure 23 were obtained after 1 hour and 25 minutes of NP incubation.

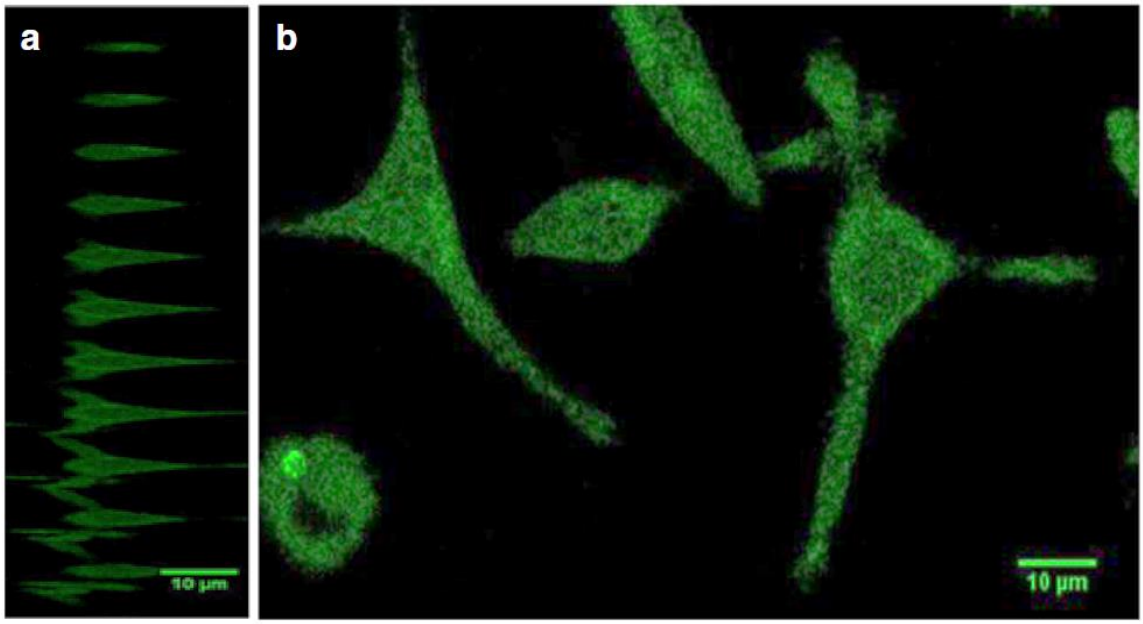

Figure 24. Fluorescent confocal microscopy image of the rat basophilic leukemia cells. a) Cross-sections (z-stacks) of a cell separated by 5 micrometers, b) top view of cells as at one specific z-stack.

In living cells, the membrane selectively controls transport of ions, large bio-molecules, and NPs into and out of cell. The mechanisms of this transport depend on the size of the object being transported, and include active endocytosis/exocytosis, and passive transport (this mechanism is predominant in red blood cells). Internalization of a

NP not only depends on their size, shape, surface charge and surface chemistry [88] but also depends on the cell-specific parameters, such as cell type or cell cycle phase. [89] In this study, cells were fixed, then stained with NPs (as often performed in immunoassays), hence only passive transport could take place. According to Van Lehn et al. pore formation in the membrane can be avoided if the ligand layer on the NP is able to adjust to the membrane, allowing surface charges to rearrange, so that the NP appears hydrophobic. [90] As the ligand layer around smaller particles contains a large amount of free volume because of the high curvature, ligand fluctuations are maximized, allowing small NPs to more easily penetrate a membrane. [91] We note that another possibility of NP internalization in this study is the partial permeabilization of a cell membrane by paraformaldehyde. According to Ref. [92] , generally, cells are fixed with paraformaldehyde, which stabilizes the membrane and *increases its permeability*, and the cells are further permeabilized with another agent (if needed). Further study of the size-dependent NP internalization by live cells would be of great interest.

3.6 Toxicity of NPs towards RBL cells

A total of 7×10^4 Rat Basophilic Leukemia (RBL) cells were cultured per well in a 24- well tissue culture plate. After a 17-hour incubation period, aqueous suspensions of silver nanoparticles with specified NP concentrations (0.005, 0.05, 0.5, 5, and 50 nM) were added. These concentrations correspond to 0.01, 0.1, 1, 10, and 100 μM silver atom concentration, assuming one 10 nm NP contained 5×10^4 silver atoms. Pure cells, without the addition of nanoparticles were used as a control. The numbers of cells in each well were then counted at hour 15, 27, 39, and 58, after the silver nanoparticles

were added. The data were acquired in triplicate. Figure 25 shows that NPs were non-toxic up to a 10 µM silver concentration and inhibited cell proliferation at a concentration of 100 µM.

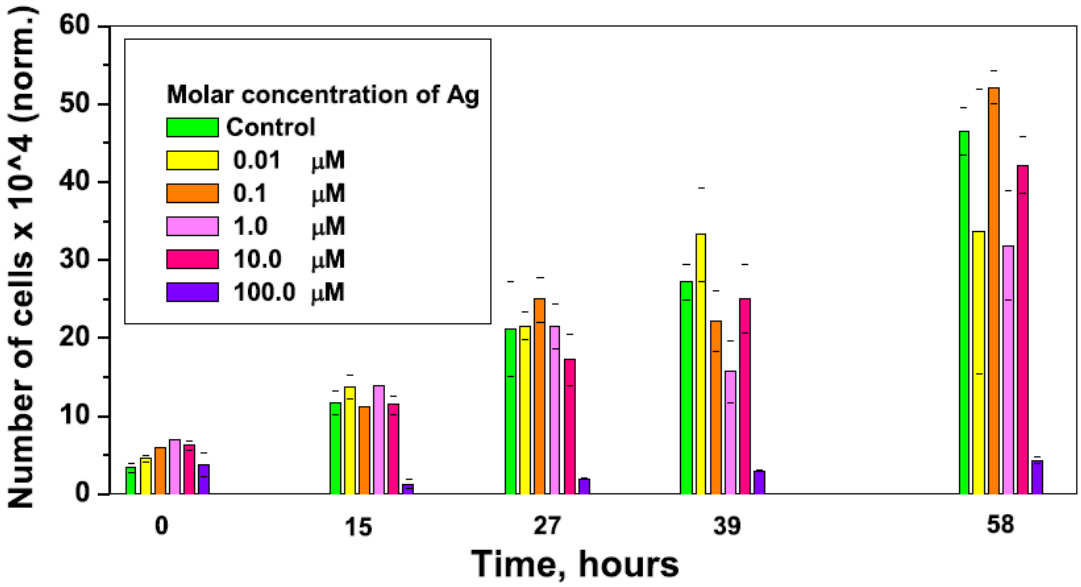

Figure 25. Proliferation of the RBL cells incubated with silver nanoparticles colloids of different concentrations.

Silver NPs are known to have antibacterial properties. [93] They are toxic towards bacterial cells, but non toxic towards mammalian cells up to relatively high concentrations (toxic effects start when Ag NPs concentration reaches ~200 nM, according to Ref. [94]). This property of NPs is becoming more of interest, as antibiotic-resistance in bacteria has become a major clinical and public health problem. [95] The main mechanism of NP toxicity is inhibition of the cell proliferation due to NP decomposition into Ag^+ ions. This decomposition is a result of dissolution of NPs in the liquid medium, [94] and digestion of NPs upon intercellular uptake. Ag^+ ions can bind to thiol containing molecules within the cell. [96] It has been shown that it leads to cell

membrane detachment from the cell wall, cell wall damage, cell shrinkage and dehydration, and stress response via accumulation of DNA in the center of the cell. [97] In Escherichia coli bacteria, silver NPs cause cell proliferation inhibition. [93] Minimal inhibition concentration of Ag NPs has been determined to be 3.3 nM, which is relatively low compared to the Ag NPs concentration in our study (compare to 50 nM, for which the toxic effect was observed).

Furthermore, other studies report toxicity of silver NPs (versus Ag^+ ions) on mammalian cells showed significant toxic effects starting from 200 nM NP concentration, [94] which suggests that our NPs are more toxic. Literature also suggests that other effects on the rat basophilic leukemia cells, such as degranulation, may occur. [98]

3.7 Etching NPs: removing NPs from the cell's surface after imaging

One of the current issues in studies of toxic and allergic effects of NPs towards living cells is differentiation between the NPs which have penetrated the cell membrane, those attached to the surface of a cell, and those which are free floating in the cell media or attached to a substrate. [55] I show in this section that our fluorescent NP probes (sample of average 9 nm diameter NPs) may be readily removed from the substrate and media, and most likely from a surface of the cells via bio-friendly etchant solution. First, I present that silver NPs can be successfully etched (dissolved) in water, phosphate buffered saline (PBS) and cell growth media. Scattering spectra of silver NPs coated with fluorescent pyrazine derivatives (glycine dimers) in water are presented in Figure 26 (a).

The black curve represents colloid before etching, and the grey curve – after etching. Figure 26 (b) shows scattering spectra of the same colloid NPs in cell growth media. The dark yellow curve represents NPs before etching, and the grey – after.

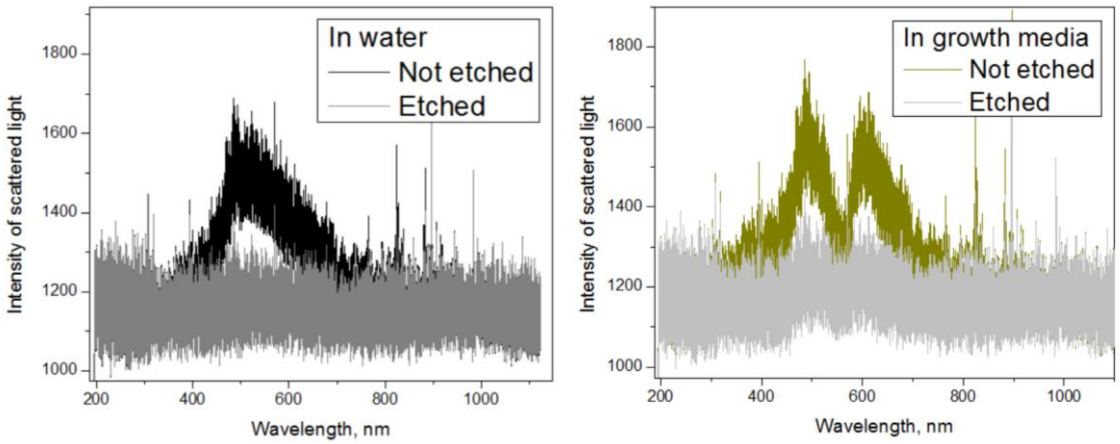

Figure 26. Scattered light intensity, registered in 90^o geometry with respect to the excitation beam. a) In water: Black – light scattered by NPs in water, grey – after addition of 0.2 mL total of etching solution to 2.2 mL of NPs in water; b) In media: Dark yellow – light scattered by NPs before etching in media, grey – after etching (same proportions as in a)).

Scattering spectra in both water and media are registered at 90^o angle with respect to the incoming light beam. Spectra show an SPR-related scattering from NPs, convoluted with the lamp intensity profile. Correction for the *spectral* profile was not critical in these experiments, since the main idea of these experiments was to show that *intensity* of light scattered by NPs drops when NPs are etched away, and hence, there is nothing there for the light to be scattered on. Light source intensity fluctuations were negligible with respect to the amplitude of the scattered light spectra. Water and growth media both have extremely low scattering compared to NPs. This can be seen from

scattering curves of both solvents after etchant has been added (grey curves in Figure 26). Both of these spectra were taken 10 min after etchant addition.

The interesting question is “how fast does etchant dissolves NPs?” The answer to this question depends on the concentration of the sample, and in our case, for 0.16 nM concentration of NPs, it is within 5 minutes (Figure 27). Different colors of curves represent the times after etchant has been added. Black curve shows scattering spectrum of NPs in PBS before etchant addition.

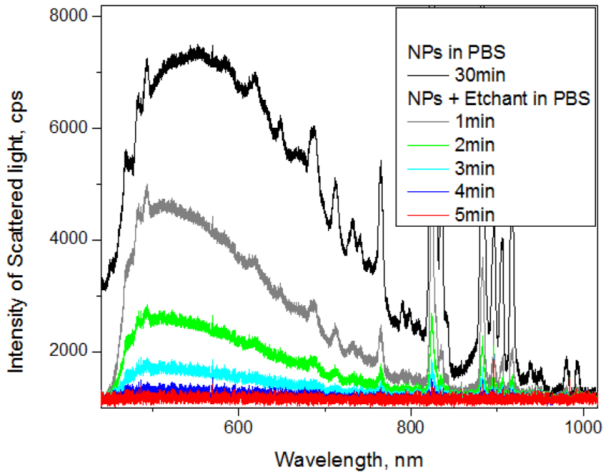

Figure 27. Etching kinetics for NPs in PBS. Black curve – no etchant added, grey – 1 min after etchant addition, green – 2 minutes, cyan – 3 minutes, blue – 4 minutes, red – 5 minutes.

We can dissolve NPs in water, PBS, and media, but can we remove NPs from the substrate (microscopy slide, or bottom of a well) after cell imaging? And can we remove NPs from the surface of a cell, while leaving NPs inside a cell intact? Next, I show confocal microscopy and spectroscopy data in attempt to answer these questions.

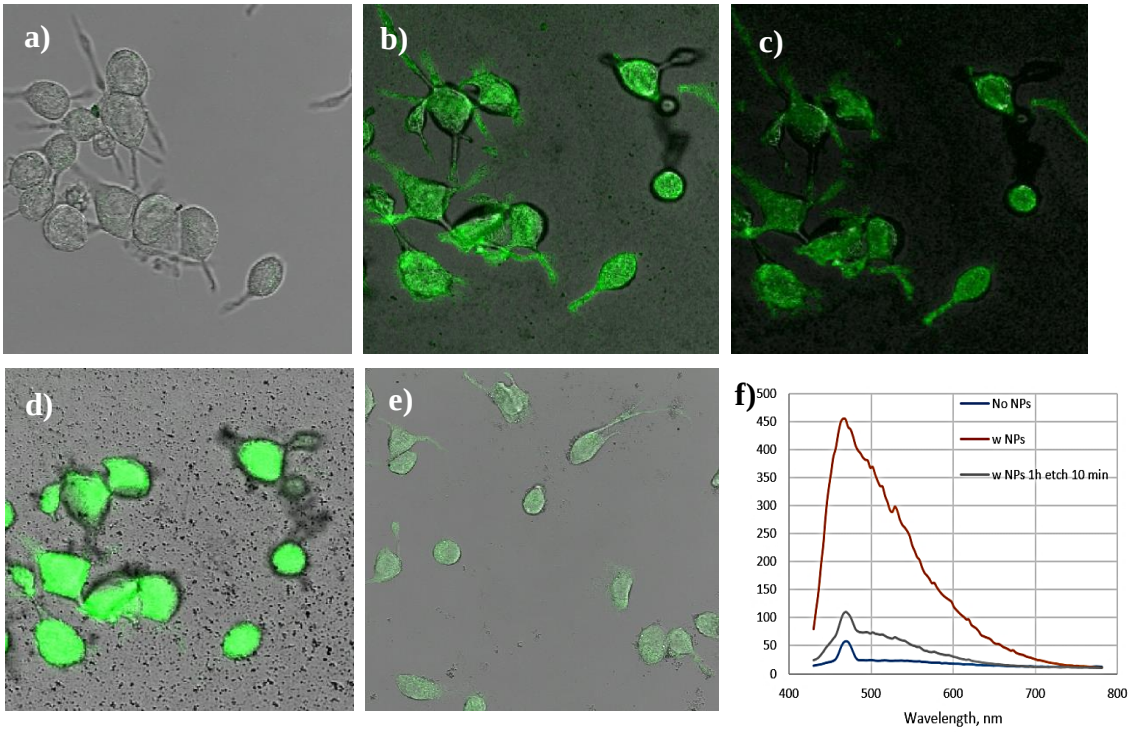

Figure 28. Confocal fluorescence microscopy images of fixed RBL cells with glycine-dimer-NPs. PL of dimers excited at 405 nm, and registered at 460 nm (except (d) – registered at [420 - 780] nm range). (a) Cells in PBS, no particles added, (b) 10 min after NPs added to the cells, (c) 20 min after NPs added (d, e) 1 hour after NPs added, followed by 10 min of etching, and then wash with PBS. (a-d) same cells were imaged. (e) different area in the same well. (f) PL emission spectra obtained from images (a) – blue curve, (b) – red curve, and (e) – grey curve.

Figure 28 (a) represents florescent confocal microscopy of cells in PBS without NPs. Weak PL signal (autofluorescence) can be seen in green (a), and a blue curve in Figure 28(f) corresponds to this signal. After NPs were added to cells, PL signal was strong both in confocal image (Figure 28 (b)), and in PL spectrum (red curve in Figure 28(f)). The background on images (b-d) is darker than in (a, e). This is due to laser-assisted deposition of NPs (formation of aggregates under UV illumination). This process has previously been reported by our group. [99,100] NPs aggregates absorb light and

therefore the background looks darker. After 20 min of incubation, Figure 28 (c), most of the light is absorbed by the aggregates of NPs, and PL is visible only from the cell areas. This suggests that aggregates are formed less effectively on a cell surface, than on a glass substrate. After an hour of incubation of cells with NPs, etching solution was added. Solution proportions were as described in the literature. [55] Then after 10 min of etching cells were washed repeatedly with PBS and Figure 28 (d) was obtained. One can see that etching removed a lot of aggregates, and the background looks much lighter. Longer etching times may be needed to remove some of the aggregates, which were still present on a substrate. The reason PL from the NPs within the cells in Figure 28 (d) appears much stronger than in the rest of the images is because for this figure PL was collected from the whole spectral range, [420 – 780] nm, as opposed to the rest of the images, where PL is registered at 460 nm only.

To compare the area, where NP deposition did take place, I obtained Figure 28 (e) by moving the objective away from the area where (a-d) were taken. This are was not illuminated by UV light at any previous point, and was within the same well, hence all cell treatments were consistent. For this area no PL signal is visible on a substrate, but some signal is present from the cells. The PL spectrum obtained from this image is shown in Figure 28 (e), by the grey curve.

In summary, the comparison of images (a) vs (b), and corresponding blue vs red PL spectra in (f) of Figure 28, demonstrates how much stronger NPs emission is compared to the cell's autofluorescence. Comparison of images (c) and (d) demonstrates

PL drop after NP etching. This drop in the signal is also seen from comparison of red vs grey PL spectra in (f), which were obtained from images (b) and (e).

It is also seen from the confocal microscopy images that after etching PL is still present within the cells. Therefore, NPs remain either inside the cells only, or also are attached to cell surfaces. To make a conclusion about effectiveness of the etchant towards removing surface-bound NPs (while leaving NPs inside the cells intact) additional experiments must be performed. Mainly, z-stack images need to be taken before and after etching. This may be a goal for the future studies.

3.8 Conclusions

In conclusion, a correlation between the SPR-related peaks in the extinction and intrinsic emission spectra of silver nanoparticles of different sizes has been experimentally demonstrated. It was found that for NPs with an average diameter in the range of 9-32 nm, an increase in particle size leads to a red shift of the peak in both extinction and intrinsic photoluminescence spectra. These observations expand previous studies, and prove the role of the SPR in the PL of noble metal NPs. The intrinsic particle PL emission is rationalized via radiative damping of the surface plasmon.

The nanoparticles were functionalized with fluorescent glycine dimers. The intrinsic photoluminescence of the particles was orders of magnitude weaker, and was spectrally separated from the photoluminescence of the glycine dimer ligands. The spectral position of the ligand emission was independent of the particle size, however the quantum yield of the nanoparticle-ligand system was size-dependent. This was attributed to the enhancement of the ligand's emission caused by the SPR

dependence on the particle size. The maximum quantum yield determined for the (23 nm diameter NP)-ligand complex was (5.2 +/- 0.1) %.

Additionally, it was shown that NPs with average diameters of 9 +/- 4 nm can be used for bio-imaging of fixed C17.2 neural stem cells as well as rat basophilic leukemia, RBL cells. The nanoparticles were able to penetrate cell membranes of rat basophilic leukemia and neural stem cells fixed with paraformaldehyde. Toxicity studies were performed. It was found that toward rat basophilic leukemia cells, luminescent silver nanoparticles had a toxic effect in the silver atom concentration range of 10 – 100 μM.

Preliminary experiments on removing NPs from the sample after bio-imaging showed promising results: particles are etchable in water, phosphate buffered saline, and cell growth media. In phosphate buffered saline NPs etched away within 5 minutes. Confocal fluorescence imaging and spectroscopy suggests NP removal via etching from the substrate, and possibly surface of the cells (additional experiments are required), while leaving NPs within the cell intact.

CHAPTER IV

OPTICAL PROPERTIES OF GOLD FILMS OF DIFFERENT MORPHOLOGY: IS THE EFFECTIVE MEDIUM APPROACH EFFECTIVE?

4.1 Introduction

Surface plasmon polaritons, introduced in Chapter 1, are elementary excitations involving the coupling of electron density oscillations (typically in a metal) with an electromagnetic wave [101,10,11]. A primary tool to excite and measure these waves is the technique of attenuated total reflection, ATR. The sensitivity of the ATR signal to the changes of the dielectric constant of the medium adjacent to the gold film enabled the emergence of the field of plasmonic bio-sensing [2]. While uniform films with a bulk-like dielectric function are widely used in bio-sensing, island-like thin films are utilized in solar cells [102]. Other applications for the island-like films include biosensing, cellular imaging, cancer cell detection, and surface enhanced Raman scattering [103,104,105,106,107].

In this chapter I present use of multiple experimental techniques (light transmittance, attenuated total reflection, atomic force microscopy, and profilometry) and corresponding theoretical calculations to see if there is a possibility to obtain a good theory-experiment match for any film morphology, using effective medium parameters. I measured both ATR and transmittance for a series of thin Au films, varying in thickness from about 5.5 nm to 55.8 nm. Then experimental results are compared with the results of theoretical calculations involving both a bulk metallic material (with optical constants taken from Johnson and Christy [108]) and with an effective medium to represent a rough

metallic material. In particular, the behavior of a two-layer system is calculated, one layer with a bulk dielectric function to represent a uniform metallic under-layer, and an effective medium layer to represent an inhomogeneous metallic layer (Figure 29).

Figure 29. Sketch of a 2-layer model for our films. Upper inhomogeneous layer, with high roughness, modeled with effective medium theory, and lower uniform layer, modelled using dielectric function for bulk gold.

The thickest films (35.8 nm and 55.7 nm) can be well described by a single bulk film using the bulk dielectric constants. Intermediate thicknesses (20 nm – 26 nm) can be properly characterized by a double layer system with a bulk layer and an effective medium layer with a thickness consistent with atomic force microscopy (AFM) measurements. Finally, the thinnest films show different behavior and cannot be described by simple models with an effective medium where air is included within a metallic matrix. This is an indication that localized excitations, not contained in an effective medium description, may play an important role.

4.2 Background

The coupling of the electromagnetic field with coherent electron oscillations at a metal surface results in the propagation of a surface plasmon-polariton (SPP) along the metal/dielectric interface. The condition for the excitation of a SPP, is matching the frequency and parallel wavevector of the incident electromagnetic field with those of the surface plasmon.

The dispersion relation for SPPs localized at a plane interface between a semi-infinite metallic and a dielectric media follows directly from Maxwell's equations:

$$(k_{spp})_x = \frac{\omega}{c}\sqrt{\frac{\varepsilon_m \varepsilon_d}{\varepsilon_m + \varepsilon_d}} \tag{19}$$

where $(k_{spp})_x$ is the parallel component of the wavevector of a surface plasmon and ε_m and ε_d are dielectric constants of the metal and dielectric, and c is speed of light. Since the dielectric permittivity of the metal and dielectric both determine the value of the surface plasmon's wavevector, the condition for the excitation of the SPP is also dependent on these dielectric constants. Additionally, we have the wave vector of the incident light, which depends on the frequency (energy) of the light. For the light travelling in a dielectric prism, often used in ATR experiments,

$$\left(k_{ph}\right)_x = k_{ph} cos\theta_i = \frac{\omega}{c}\sqrt{\varepsilon_p} \tag{20}$$

where ε_p is a dielectric constant of the prism and k_{ph} is the wavevector of the incident light in the prism at an angle θ_i. When the two vectors (Equations 19 and 20) match – a surface plasmon polariton is excited.

For the films with rough surfaces and island-like non-uniform films an effective medium approach could be used to describe their optical properties. A good summary of effective medium approaches involving thin films was presented in 1976 by Jarrett and Ward [109]: here a comparison of theoretical and experimental results was used to determine the shapes of particles in the films and a discussion of various effective medium theories (Maxwell-Garnett, David, Yamaguchi and Polder and Van Santan) was also presented.

Following this, Norrman [110,111] first studied the optical transmittance in thin films, 0.3 – 2 micrometers thick, followed by a study of the transmittance in discontinuous (island-like) gold films of 1.3 – 3.6 nm thickness. The Maxwell Garnett formalism was utilized to describe the absorption, taking into account the size-dependence of the dielectric permittivity of the islands. They concluded that optical properties of films were governed by the morphology of the islands and dipole-dipole interactions between them.

4.3 Reflectivity and Transmittance Measurements

A three-dimensional view of the geometry of the experiment is presented on Figure 30 (a). A Xenon lamp with a monochromator was used as the light source. Light enters the prism, and after traveling through the index-matching oil and glass substrate is reflected off an Au film. The prism, made of BK7 glass, was mounted on the rotating stage (axis of rotation is shown on Figure 30 (a)) such that the angle of incidence could be changed with 0.1^{o} precision. The incident wavelength of the light was in the [510 – 780] nm range and 30 nm intervals were used to measure the ATR signal. The incident light was polarized parallel to the plane of incidence. The intensity of reflected light (I_r) was registered at different incidence angles, relative to the normal to the gold surface (angle Θ in Figure 30 (b)). Incidence angle was determined via back-reflection test with $\pm 0.5^{o}$ error.

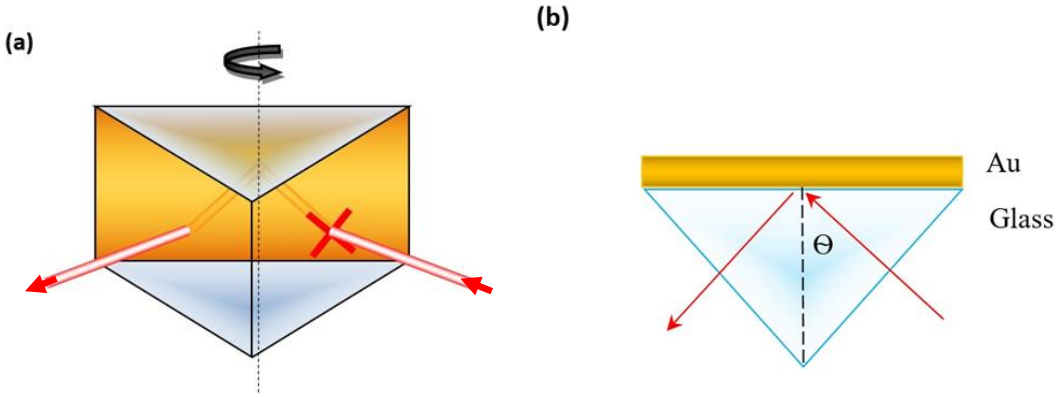

Figure 30. Sketch of the ATR experiment. (a) shows a 3D view of the geometry with the axis of rotation, passing through a vertical back side of a prism. (b) TM polarized light enters the prism, creating an angle θ with the normal to the gold surface.

The intensity of the light reflected from the gold film, I_r was a maximum at the $\Theta = \Theta_c$, the critical angle, corresponding to total internal reflection. Our prism had an index of refraction of n = 1.517 giving a critical angle of 41.2 degrees. Intensity of reflected light was minimal at the $\Theta = \Theta_{SPP,}$ corresponding to the excitation of the surface plasmon polariton at the interface between the prism and the gold film. We chose to measure the ATR around this angle $\Theta_{SPR} = 45^o$. Light transmittance spectra were measured on a Perkin Elmer double-beam spectrometer. Illumination was from the glass side of a sample, and plain glass was used as a reference.

4.4 Thickness and morphology characterization

Gold films were deposited onto glass slides under vacuum using a Denton Vacuum sputtering chamber. Glass slides were repeatedly cleaned in a sonicated bath in a 2% volume detergent/water solution for 15 min, rinsed with distilled water, then ethanol, and blown dry in nitrogen. Film thickness was controlled by the deposition time.

A Veeco Multimode atomic force microscope (AFM) was used to characterize the film roughness and morphology. This data was then used to estimate the volume fill fraction parameter used in our theoretical calculations. Additionally, the AFM data was used for all film thickness estimates by analyzing the profile of the film adjacent to the location of all transmittance and ATR measurements. Morphology of the films is represented in Figure 31.

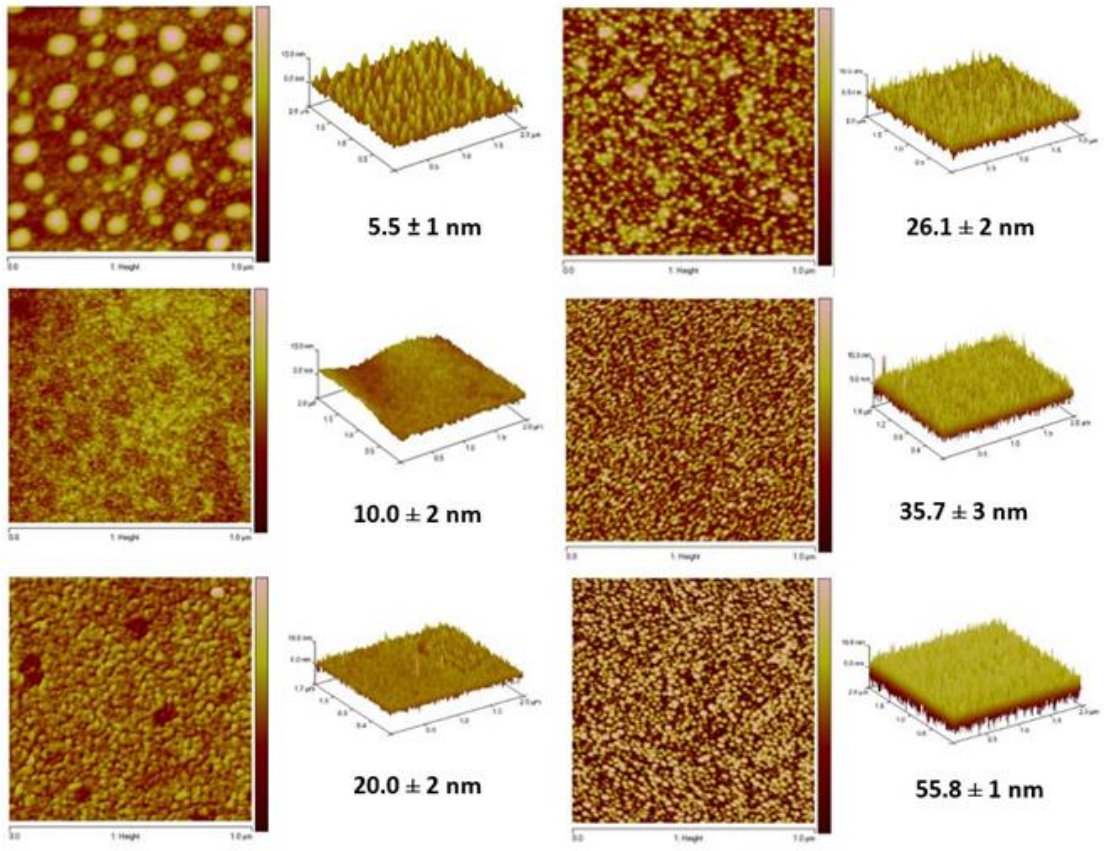

Figure 31. Atomic force microscopy images for gold films. In the top view image depths range was 0 – 10 nm. The scan size is 1 micrometer. The 3D height is ± 10 nm in z, and the x, y axis is 0 – 2 micrometers (except for 20 and 35.7 nm y is 0-1.7).

As one can see from Figure 31, film grain size decreases as the film thickness increases. The island-like film of 5.5 nm thickness has grains, which largely vary in size. At the same time a film of 55.8 nm thickness has small grains of roughly the same size. A

summary of average roughness of the films, maximum surface height variation extracted from the AFM, as well as total thickness of the films extracted from the profilometry data, are presented in Table 1. T_{av} is average film thickness, ΔT_{Max} is maximum surface variation, and R_a is average film roughness. All values are in nanometers.

Table 1. Film thickness and roughness characteristics (in nm), extracted from AFM data.

T_{av}	5.5 ± 1	10.0 ± 2	20.0 ± 3	26.1 ± 4	35.7 ± 3	55.8 ± 1
ΔT_{Max}	6.0	4.2	5.4	4.6	4.8	3.2
R_a	0.62	0.79	0.84	0.65	0.42	0.37
$\Delta T_{Max}/ T_{av}$	1.09	0.42	0.27	0.18	0.13	0.06

For thinnest film, Table 1 shows that average thickness of the film, T_{av}, is approximately equal to the maximum variation of the surface, ΔT_{Max}. Therefore, this film is island-like. The rest of the films have $\Delta T_{Max} < T_{av}$, which means they have an under-layer, and an inhomogeneous over-layer. Hence, double-layer model is appropriate for all films, except for the thinnest island-like film of 5.5 nm thickness.

4.5 Light transmittance: experiment and theory.

Transmittance spectra were calculated using Fresnel coefficients for the slab [112] The effective permittivity for the second layer was calculated with the Maxwell-Garnett effective medium theory (MGT). [8]

$$\epsilon_{av} = \epsilon_m \left[1 + \frac{3f\left(\frac{\epsilon - \epsilon_m}{\epsilon + 2\epsilon_m}\right)}{1 - f\left(\frac{\epsilon - \epsilon_m}{\epsilon + 2\epsilon_m}\right)} \right] \tag{21}$$

where ϵ_{av} is the average effective permittivity, ϵ_m is the dielectric permittivity of a matrix (gold in our case), ϵ is the permittivity of inclusions (air in our case), and f is the volume fraction of inclusions.

$$f = \frac{v}{V} \tag{22}$$

where v is the volume of inclusions, and V is the volume of matrix. Hence, $f = 0$ for pure gold.

A fit of the experimental data is presented in Figure 32. The MGT requires that volume fractions for spherical metallic inclusions remain low such that there are distinct conductive domains in the effective medium. To meet this requirement, we kept the fill factor of metallic inclusions below f = 0.25 [113] for thicker films (Figure 32).

Figure 32 (a) shows the experimental and theoretical transmittance results. The calculated curves were obtained using thicknesses and fill factors of the 1st (uniform) and 2nd (rough) layer as follows:

(Red curve, 55.6 ± 1 nm) - 1st layer was 53 nm of bulk gold (f=1), and 2nd layer was 2 nm of gold-air effective medium (f=0.2). This corresponds to a total of 55 nm, which is in good correlation with the experimental 55.6 ± 1 nm. The film thickness to maximum surface variation, $\Delta T_{Max}/ T_{av}$ of 6%, and average roughness, R_a of 0.37 nm supported our choice.

(Orange curve, 35.7 ± 3 nm) - 1st layer was 32 nm of bulk gold and 2 nm of effective medium (f = 0.25) was the 2nd layer. Therefore, the total of 34 nm layer model was also in good correlation with experimental the 35.7 nm within ± 3 nm error.

(Dark yellow curve, 26.1 ± 1 nm) was modeled by 24 nm of bulk gold (f = 1) and 2 nm of f = 0.25 effective medium (total of 26 nm). (Unless otherwise indicated *f* refers to the filling fraction of air in Au matrix.)

Correspondence between theory and experiment is good for all three film thicknesses, which is the expected result, taking into account roughness of the films, and therefore a thin effective medium layer used to model such roughness.

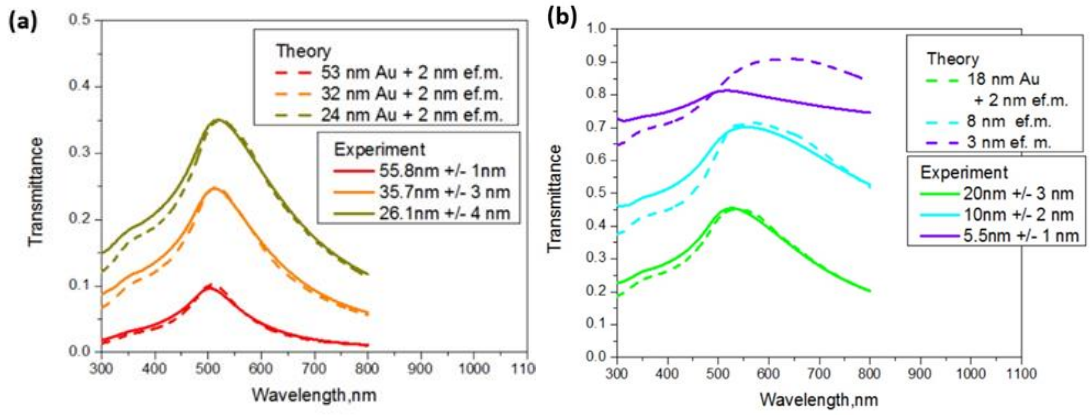

Figure 32. Experimental transmittance vs wavelength of the incident light on the glass/gold interface (Solid lines). Theoretical data is represented by the dashed lines. Different colors represent different thicknesses of the film. (a) shows results for thicker films where theory and experiment agree well, and (b) presents the results for thinner films. In the thinnest two films it was not possible to obtain good agreement.

In Figure 32 (b) model parameters were following:

(Green curve, 20.0 ± 3 nm) - The 1st layer was 18 nm of bulk gold and the 2nd layer was 1 nm of effective medium with *f* = 0.25 (total of 19 nm). This film, with a 0.84 nm roughness and 27% of thickness/surface variation, was the least uniform among the 4 films modeled by a double-layer.

Films of thicknesses 10.0 ± 2 nm and 5.5 ± 1 nm were not modeled well by the double-layer model with MGT where the effective medium layer was thicker than the under-layer (Figure 32 (b)). It was difficult to model the transmittance for the thinnest

films. Surprisingly, the best results were obtained with a single effective medium film, slightly thinner than the actual film, with a filling fraction of 0.02. Variation from f = 0.02 to f = 0 led to a substantial difference in the transmittance curves.

4.6 Attenuated total internal reflection.

A schematic representation of the ATR experiment is shown in Figure 33. We solve Maxwell's equations and boundary conditions for the electric and magnetic fields from p-polarized (TM) light propagating in four media: the prism, bulk metal, effective medium layer and air. [114]

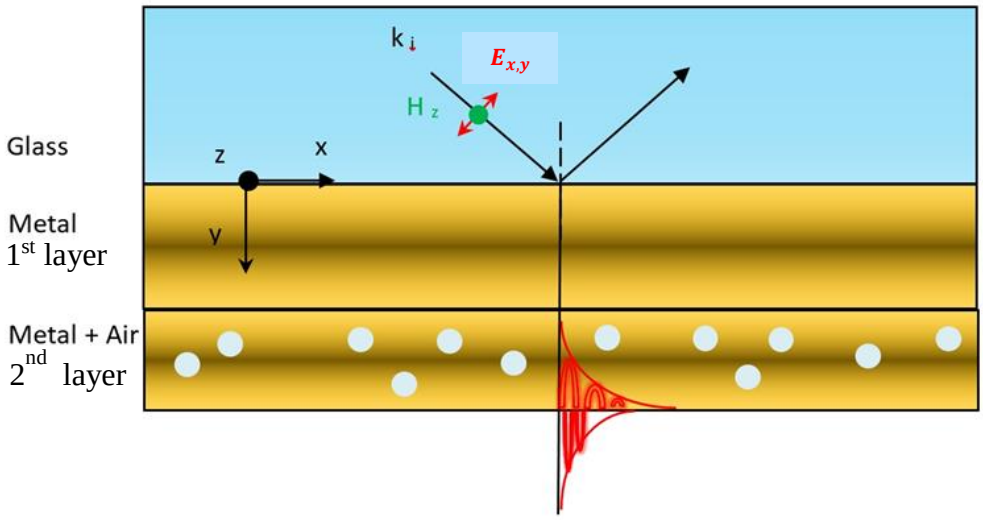

Figure 33. Sketch of the ATR geometry and electromagnetic fields. The SPP (shown in red) is localized at the boundary of the effective medium film and the air.

The coordinate system is chosen such that the TM polarization of the incident light has a nonzero component only in the z direction ($H = H_z$). The vector of the electric field consequently has a z-component equal to 0 ($E_z = 0$). In Figure 33 k_i represents the wavevector of the incoming light and $E_{x,y}$ is a projection of the electric field vector onto x axis.

Solving for the electric fields in each region and setting the incident field intensity to 1 yields a value for the ATR reflectance [101]. The calculated reflectance is then compared to the experimental measurements that have been modified by the Fresnel equations [8] to account for reflections as the beam is entering and exiting the prism. Comparisons of the experiment and theory are shown in Figure 34.

Figure 34 shows the ATR data at an angle of incidence of 45.8 degrees. The red curve corresponds to the thickest film (55.8 ± 1 nm) and has a characteristic dip around 570 nm. It is associated with the surface plasmon polariton. More pronounced SPP dip was observed for the 35.7 ± 3 nm film (orange curve). The dip shifts to the longer wavelength as film thickness decreases. The film of 26.1 nm thickness (dark yellow) also supports SPP, however the dip is much broader and is shifted towards the longer wavelength (630 nm).

As films become thinner the ATR signal approaches 1, total internal reflection, since we are measuring reflected light at an angle of the incidence greater than the critical angle. However, for the thinnest film (5.5 nm, purple curve) the wavelength dependence is quite non-monotonic, which can be rationalized by the excitation of the localized surface plasmons, supported by islands in such film (see AFM image on Figure 31).

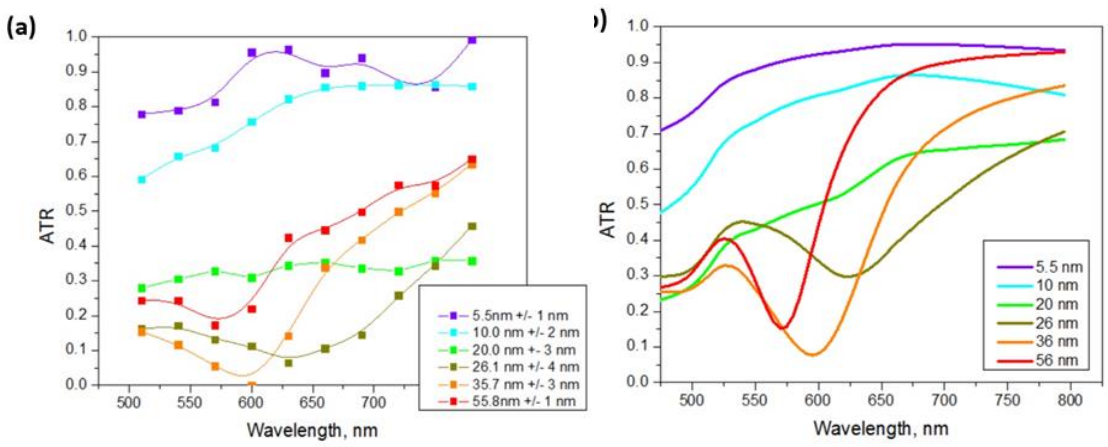

Figure 34. ATR dependence on the wavelength of the incident light. Different colors of the curves represent film thickness. a) experiment, b) theory.

The permittivity values used for the ATR theory calculations are consistent with those used in the transmittance calculations above. Again, we see that the characteristics of the thicker films (55.8 nm and 35.7 nm) are modeled well by a continuous film with a small effective medium layer on the outside. However, for the thinner films we see that the theoretical effective medium model fails to capture the excitations (the individual peaks and dips) found in the experiment. This suggests that the cause of the excitations in the thin films has changed from SPPs to localized plasmons in the island-like morphology. As the effective medium calculation treats the film as a continuous layer with a single permittivity value it cannot accurately model localized plasmons.

As the film thickness is decreased we first see a wavelength broadening of the SPP dip followed by a decrease in the magnitude of the SPP dip. This is expected for films thinner than a critical thickness (around 50 nm) as the coupling between the evanescent field and the electron response of the thin film decreases [115].

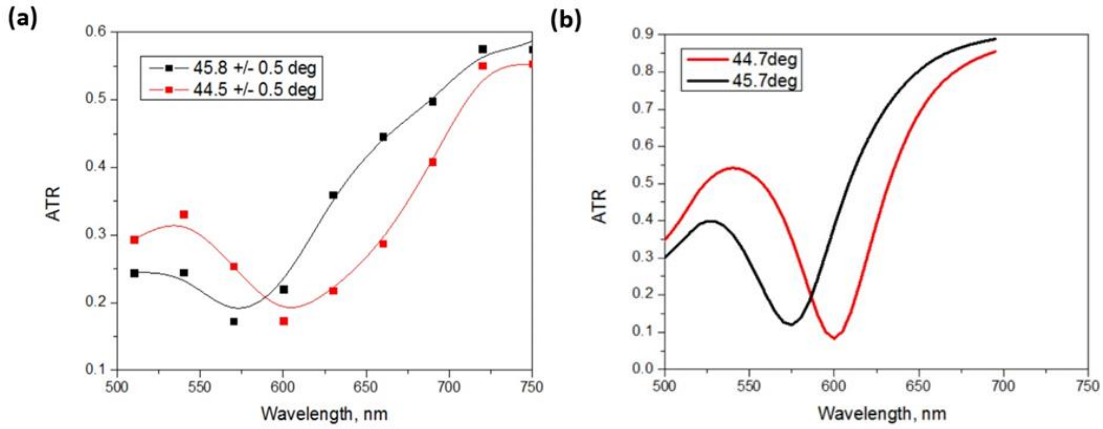

Figure 35. a) Experiment, and b) theory for ATR dependence on the wavelength and angle of the incident light for 55.8 nm film. Different colors of the curves represent different incidence angle.

The angular dependence of the ATR is presented in Figure 35 for the 55.8 ± 1 nm film. The SPP-related dip shifts towards longer wavelengths as the angle of incidence increases (compare black vs red curves). The angular dependence of the SPP dip is also evident in the calculated ATR curves (Figure 35 (b)). It can be understood via matching the projection of the light wave vector (which is determined by the angle of incidence) to the wave vector of the surface plasmon, as was described in the background section. Note that while the horizontal scale in Figure 35 is the same, the vertical scale is different. This is because we excite our SPP with ± 15 nm wavelength (due to limitations of the monochromator), and theory doesn't take this into account. The SPP dip position is reproduced well by theory: it is around 575 nm for 44.7^{o} incidence angle, and 600 nm for the 45.7^{o} angle.

4.7 Theoretical calculations of the attenuated total internal reflection and transmittance

As discussed in the Background section, an SPP can be excited when the incident wavevector of the light matches the wavevector of the surface plasmon, or after some simplification

$$\varepsilon_p = \frac{\varepsilon_m \varepsilon_d}{\varepsilon_m + \varepsilon_d} \tag{23}$$

To satisfy the equation above we require a negative permittivity material (the Au film) adjacent to a positive permittivity material (the dielectric).

A number of changes can occur by placing an effective medium material between the Au film and the dielectric layer. Figure 36 (a) shows the change in permittivity using MGT for an effective medium Au film with a volume fraction of $f = 0.2$ air inclusions. The real part of the permittivity has decreased in magnitude, but the characteristics of the Au permittivity are still evident. In contrast, when using MGT for an effective medium dielectric film with $f = 0.2$ Au inclusions in air (seen in Figure 36 (b)) we see that there is a change to the magnitude of the real part, but it remains positive.

In both cases the sign of the permittivity in the effective medium regime does not change, and so we are not creating a new surface to allow propagation of an SPP. Thus, we do not expect new peaks or dips (like those seen for the 5.5 nm film, the purple line in Figure 34(a)) to appear in the ATR calculations as we are not creating a new condition to excite the SPP. Instead, the effective medium layer causes a change in the wavevector of the allowed SPPs and we see the SPP dip at a different frequency. This leads to the

conclusion that the 5.5 nm film must have a localized surface plasmon which cannot be modeled by the MGT in a continuous film.

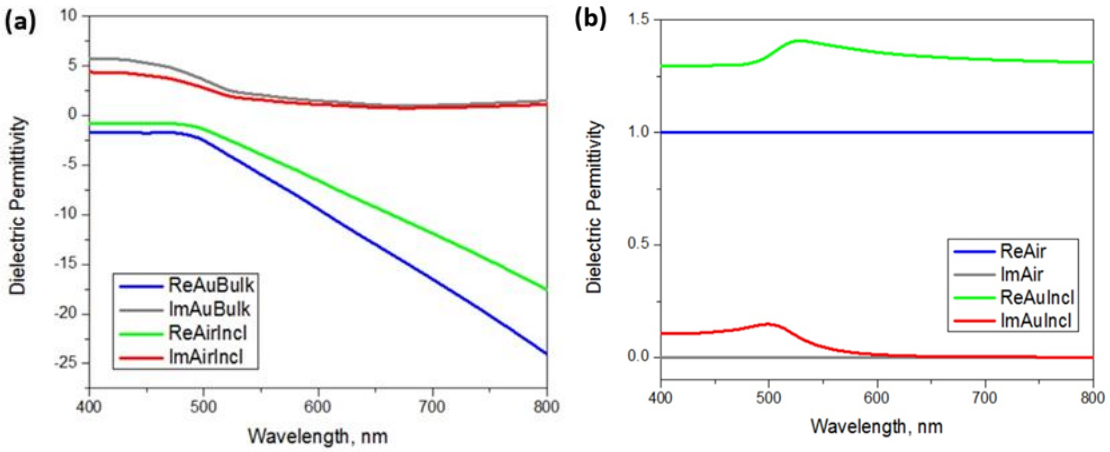

Figure 36. a) The real and imaginary components of the permittivity for a *uniform Au film*, denoted as "ReAuBulk" (blue) and "ImAuBulk" (grey), and for an effective medium with *air inclusions*, denoted as "ReAirIncl" (green) and "ImAirIncl" (red). b) The real and imaginary components of permittivity values for a *uniform dielectric*, denoted as "ReAir" (blue) and "ImAir" (grey), and for an effective medium with *gold inclusions*, denoted as "ReAuIncl" (green) and "ImAuIncl" (red). The filling factor of inclusions is $f = 0.2$ in both panels.

This raises the question, "how sensitive should the transmission and ATR experiments be to the thickness of the effective medium film?". In Figure 37 theoretical predictions for transmittance and ATR spectra are shown for different thicknesses of the effective medium layer (2nd, "rough" layer), while keeping the 1st uniform bulk under-layer at fixed thickness of 36 nm. One can see that for the transmittance graphs only the amplitude changes, dependent on the thickness of the effective medium layer, while for the ATR both the intensity and the position of the SPP dip change.

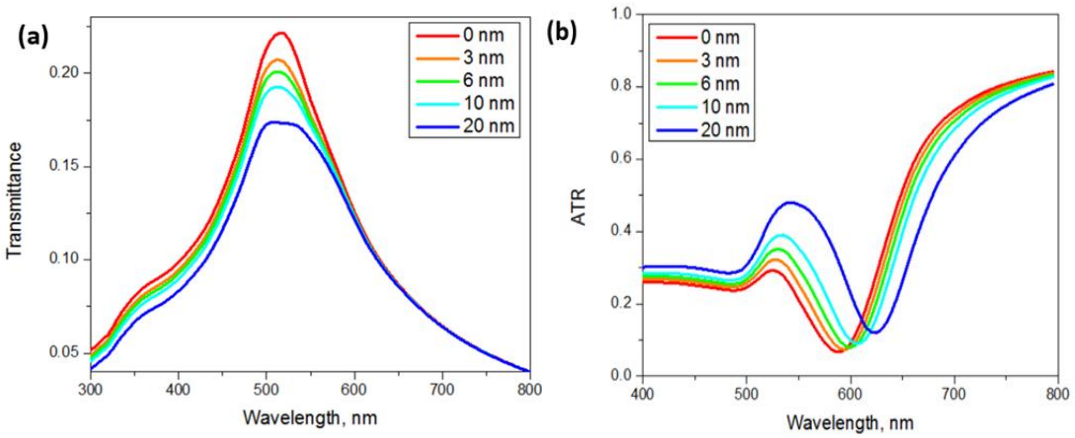

Figure 37. Theoretical calculations of change in (a) transmittance and (b) ATR signals with the thickness of an effective medium film on top of a 36 nm bulk Au film. Different colors of curves correspond to different thickness of an effective medium layer: red – inhomogeneous "rough" layer is absent, orange – "rough" layer thickness is 3 nm, etc.

4.8 Application of ATR in bio-sensing

According to Equation 20, the SPP excitation, and therefore an ATR dip position, depend on the angle at which light is incident on the gold substrate. This angle dependence provides information about the index of refraction of the bio-chemical sample adjacent to the gold film. Further I present ATR data, obtained using a prototype of the SPP sensor. The sensor was assembled on a custom-build Kretschmann geometry experimental setup for the ATR measurements with less than .001 refractive index units sensitivity. The sensor was tested on the following bio-chemical samples: 0.6 mM thiol (2-mercaptoethanol) solution in ethanol, 100 μg/mL DNP-BSA (Albumin from Bovine Serum (BSA), 2,4-Dinitrophenylated) in PBS (Phosphate-buffered saline), and 1 μg/mL DNP-IgE (Immunoglobulin E) molecules in PBS. Thiol molecules were chosen for testing because they have a high affinity to gold, and play the role of glue, providing a platform for BSA and IgE molecule attachment. Gold-thiol surfaces are widely used in commercial SPP-based bio-sensors. [116]

To confirm successful functionalization of gold films with thiol molecules, AFM was performed on the film after 20 hours of functionalization. Figure 38 presents comparison of the AFM images of thiol-functionalized vs not functionalized 50 nm gold films. Images of the non-functionalized gold surface reveal gold grains (Figure 38(a)). Images of the thiol-functionalized gold show non-uniform molecular coating on the gold surface, which makes almost impossible to resolve the separate gold grains (Figure 38 (b)).

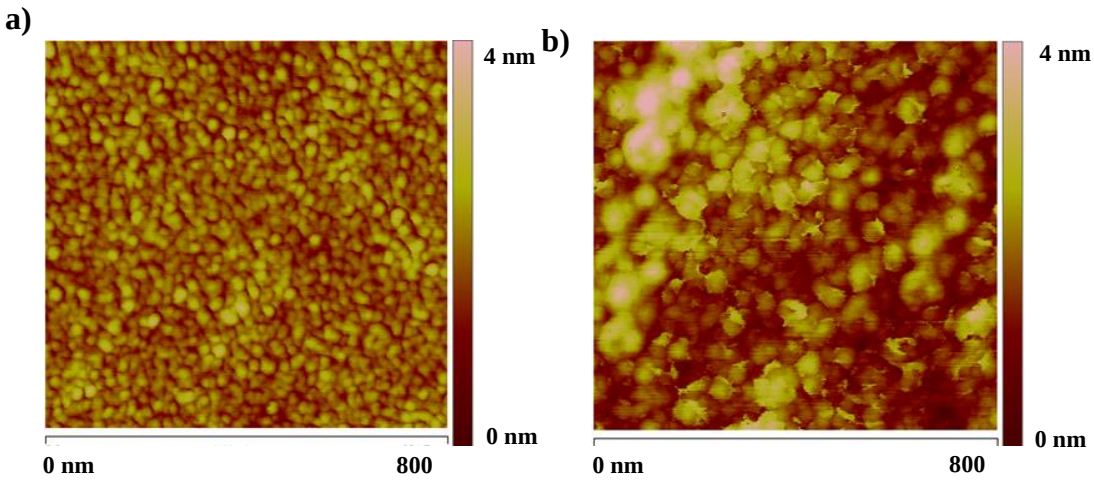

Figure 38. AFM Height images of a) not functionalized gold film, b) thiol-functionalized gold film.

ATR shown in Figure 39 (orange curve) was obtained after 20 hours of incubation of thiol solution with the gold film (same samples which were characterized with AFM, shown in Figure 38). After thiol functionalization gold film was rinsed with ethanol, and then with PBS, to prepare a substrate for further functionalization. Since the orange curve had dip at 73.05^{o}, a detector was placed at that angular position, and DNP-BSA solution in PBS was added immediately after PBS rinse. It was expected to see real-time BSA layer formation, indicated by the increase in intensity of ATR signal at a fixed 73.05^{o}

angle (inset in Figure 39). This increase is a result of a real-time change of the index of refraction of a medium adjacent to the thiol-functionalized gold film. The ATR intensity plateau indicates that a BSA monolayer has formed. According to literature, this should be expected on the order of [90 - 180] seconds (depending on concentration of BSA), after the initial introduction of the BSA to the flow cell. [117] Our experiment indicates BSA layer formation within ~ 140 s.

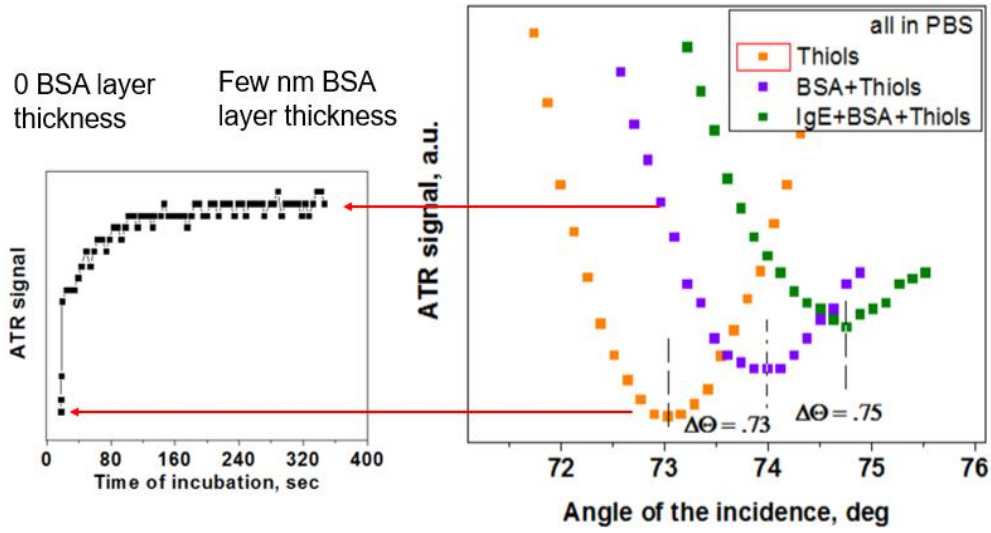

Figure 39. ATR sensing of thiol, BSA, and IgE molecular layers attached to the gold film. Inset shows ATR dynamics of a BSA layer formation on top of the thiol layer. Time of incubation denotes how much time passed since the thiol-functionalized gold surface has been exposed to a BSA solution. Red arrows indicate time ~0 sec (no BSA solution), and ~400s (BSA layer has been formed on the thiol-functionalized gold film).

As DNP-BSA layer was formed, the substrate was rinsed with PBS, and andi-DNP IgE solution in PBS was added to a flow cell. As a result, the ATR dip shifted to higher angle (Figure 39, green curve) within a few seconds. Dynamics of IgE binding to BSA was not studied here, and may be an objective for future studies. Experiments, described in this section serve as a proof of concept for sensitivity of our home-made ATR SPP sensor towards molecular binding events.

4.9 Conclusions

Combination of transmittance measurements, ATR and theoretical calculations with the use of an effective medium theory provides a good toolset for characterization of sputter-deposited gold films. Due to the methodology of the film growth, our films have a uniform under-layer and a rough over-layer (confirmed with the AFM). These films can be successfully modeled by a thick continuous layer with bulk dielectric permittivity and a thin layer on top with an effective medium permittivity. Such a fitting is not necessarily unique, but this fitting is consistent with all the experimental data, including the structural data. When the film is 10 nm or less, the transmittance and ATR spectra are no longer well modeled by a simple effective medium calculation. The SPPs are not the cause of the new features in the spectra, but more likely localized plasmons start contributing significantly at these thicknesses.

Our home-built experimental ATR SPP-based setup uses sensitivity of the ATR to changes in the refractive index of the molecules adjacent to gold films, and is capable of sensing formation of thiol, DNP-BSA and anti-DNP IgE layers on top of gold film.

CHAPTER V

FUTURE OUTLOOKS

Surface plasmons in individual NPs, coupled surface plasmons in NP chains, and surface plasmon polaritons in thin films, studied in this dissertation, all resulted from the plasma oscillations in metal confined to a nanoscale. Unique optical properties, arising because of interaction of plasma oscillations with light, deserve more rigorous studies in the future.

For example, while a first-of-a-kind 3D extinction map was produced for a large number of particles in a chain (as described in Chapter 2), the study of a 2-nanoparticle extinction map can provide useful information for scientists the who use 2-particle molecular rulers. [118] An interesting would be to see how the 3D extinction map changes as the size, or shape of nanoparticles change. For example, particles with sharp corners could serve as better SERS substrates, due to excitation of non-dipolar SPR fields in them. For such particles in a chain, the transition from near- and middle- to far-field interaction distance, d^* would be different from that which I report here (280 – 320 nm). This would require theoretical treatment of the problem with non-dipolar, but quadrupole, or higher multi-poles of the field included. A simpler goal could be precise determination of a transition distance in chain of spherical nanoparticles. It would require study of inter-particle distances in the range of (280 - 320) nm. Another prospective is to study 2D, or even 3D arrays (as opposed to our simple 1D chain model), since it would provide more tunability for bio-sensing applications.

As for future ideas for study of photoluminescent silver nanoparticles, evaluation of a domain structure in poly-crystalline nanoparticles, would shed more

light onto possible quantum-size effects, and corresponding emission of such nanoparticles. While in this study (Chapter 3) the intrinsic particle emission is rationalized via radiative damping of the surface plasmon, because of size-dependence of PL, fluorescence lifetime studies could also be informative for further understanding of a mechanism. Fluorescence lifetime of PL due to radiative decay is different from a fluorescence lifetime due to interband transitions. [45]

While in chapter 3 I showed that the quantum yield of the nanoparticle-ligand system is size-dependent, and the maximum quantum yield determined for the (23 nm diameter NP)-ligand complex was (5.2 +/- 0.1) %, it would be interesting to know quantum yield of free-standing glycine molecules. Study of the emission of free-standing glycine dimer molecules, compared to emission of glycine-dimer-functionalized NPs would allow for the quantitative description of PL enhancement factors.

In Chapter 3 I also described preliminary experiments on bio-imaging of RBL cells using silver NPs, and removing NPs from the sample after bio-imaging. The mechanism of particle penetration through the cell membranes cell allergic response and toxicity depending on the particle size are interesting questions, since issues of nano-toxicity, and on the other hand, anti-bacterial properties of silver are of importance due to antibiotic resistance of evolving bacteria. [119] Additionally, further studies of removal of nanoparticles via etching from the substrate and surface of the cells, while leaving particles within the cell intact are necessary. This would allow use of these particles for bio-imaging in vivo.

For better understanding of SPP in thin multi-layered films, and their application in bio-sensing, a broader study of effective medium parameters may be beneficial. For example, in Chapter 4 I showed how effective medium with fill factor of 0.25 of thickness [0 – 6] nm affects transmittance and ATR spectra. While we used only Maxwell-Garnett effective medium theory, other theories are available in the literature, and could describe better multi-layered, or thin island-like films. [109]

And finally, the next step after showing that our home-built experimental ATR SPP-based setup is capable of sensing formation of thiol, DNP-BSA and anti-DNP IgE layers on top of gold film, would be to study dynamic processes for molecules, which haven't been studied yet. For example, dextran brushes are materials widely used in the bio-sensing field, [120,121] however their pH dynamics are unknown. Since dextrans serve as a platform for protein binding events, it would be interesting to see if their shrinking/elongation under different pH conditions affects protein interaction.

REFERENCES

1 Brongersma M.L. Recent progress in plasmonics. Conference on Quantum Electronics and Laser (2008).

2 Anker J. N., Hall W. P. , Lyandres O. , Shah N. C. , Zhao J. , Van Duyne R. P. Biosensing with plasmonic nanosensors. *Nature Materials*, 7 (2008), 442-453.

3 Atwater H. A., Polman A. Plasmonics for improved photovoltaic devices. *Nature Materials*, 9, 3 (2010), 205.

4 Haes A.J., Zou S.L., Schatz G.C., Van Duyne R.P. Nanoscale optical biosensor: Short range distance dependence of the localized surface plasmon resonance of noble metal nanoparticles (2004).

5 Grigorenko A. N., Roberts N. W., Dickinson M. R., and Zhang Y. Nanometric optical tweezers based on nanostructured substrates (2008).

6 Jain P. K., El-Sayed M. A. Plasmonic coupling in noble metal nanostructures. *Chemical Physics Letters*, 153, 487 (2010), 4-6.

7 Brongersma M.I., Hartman J.W., Atwater H.A. Electromagnetic energy transfer and switching in nanoparticle chain arrays below the diffraction limit. *Phys. Rev. B*, 62 (2000), 16356.

8 Bohren C. F., Huffman D. R. *Absorption and scattering of light by small particle*. Wiley, New York, 1998.

9 Kreibig U, Vollmer M: Optical properties of metal clusters. Berlin, Heidelberg, Springer, Giepmans BNG, Adams SR, Ellisman M.H., Tsien R.Y. The fluorescent toolbox for assessing protein location and function (2006).

10 Kretschmann E., H. Raether. Radiative Decay of Non Radiative Surface Plasmons Excited by Light. *Z. Naturforsch*, 23 (1972), 2135-2136.

11 Otto, A. Excitation of nonradiative surface plasma waves in silver by the method of frustrated total reflection. *Z. Physik*, 216, 4 (1968), 398-410.

12 Sönnichsen C., Reinhard B.M., Liphardt J, Alivisatos A.P. A molecular ruler based on plasmon coupling of single gold and silver nanoparticles.

13 Kravets V. G., Schedin F. , Kabashin A. V. ,Grigorenko A. N. Sensitivity of collective plasmon modes of gold nanoresonators to local environment. *Optics Letters*, 35, 7 (2010), 956.

14 Jain P. K., El-Sayed M. Plasmonic coupling in noble metal nanostructures. *Chemical Physics Letters*, 153, 487 (2010), 4-6.

15 Crow M.J, Seekell K., Wax A. Polarization mapping of nanoparticle plasmonic coupling. *Opt Lett.*, 36, 5 (2011), 757-9.

16 Lal S., Link S., and Halas N. J. Nano-optics from sensing to waveguiding. *Nature Photonics*, 1 , 11 (2007), 641.

17 Atwater H., Polman A. Plasmonics for improved photovoltaic devices. *Nature Materials*, 9, 3 (2010), 205.

18 Enoch S., Quidant R., and Badenes G. Optical sensing based on plasmon coupling in nanoparticle arrays. *Optics Express* , 12 , 15 (2004), 3422.

19 Homola J. *Surface Plasmon Resonance Based Sensors*. Springer, 2006.

20 Springer T., Ermini M.L., Spakova B., Jablonky J., Homola J. Enhancing Sensitivity of Surface Plasmon Resonance Biosensors by Functionalized Gold Nanoparticles: Size Matters. *Analytical Chemistry* (2014).

21 Lambertz C. Single Particle Plasmon Sensors as Label-Free Technique To Monitor MinDE Protein Wave Propagation on Membranes (2016).

22 Zhang P., Kim K, Lee S., KumarChakkarapani., Fang N., Kang S. Augmented 3D super-resolution of fluorescence-free nanoparticles using enhanced dark-field illumination based on wavelength modulation and a least-cubic algorithm. *Nature, Scientific Reports* (2016).

23 Jackson, J.D. *Lassical Electrodynamics*. Wiley, 1999.

24 Kravets V.V., Ocola L.E., Y. Khalavka, A.O. Pinchuk. Polarization and distance dependent coupling in linear chains of gold nanoparticles. *Applied Physics Letters*, 106 (2015), 053104.

25 Kravets V. V., Yeshchenko O. A., Gozhenko V. V., Ocola L. E., Smith D. A., Vedral J. V., and Pinchuk A. O. (2012).

26 Pinchuk A. O., Schatz G. Nanoparticle optical properties: far- and near-field electrodynamic coupling in a chain of silver spherical nanoparticles. *Mater. Sci. Eng. B*, 149 , 3 (2008), 251.

27 Ford, W. H. Weber and G. W. Propagation of optical excitations by dipolar interactions in metal nanoparticle chains (2004).

28 Lamprecht B., Schider G., Lechner R.T., Ditlbacher H., Krenn J.R., Leitner A., and F.R. Aussenegg. Metal Nanoparticle Gratings: Influence of Dipolar Particle Interaction on the Plasmon Resonance. *Physical review letters*, 84 , 20 (2000), 4721.

29 Kravets V. G., Schedin F. , Pisano G. , Thackray B. , Thomas P. A. , Grigorenko A. N. (2014).

30 Tsai C.Y., Lin J.W.,Wu C.Y, Lin P.T., Lu T.W, and Lee P.T. Plasmonic Coupling in Gold Nanoring Dimers: Observation of Coupled Bonding Mode. *Nano Lett.* , 12 , 3 (2012), 1648.

31 Near R. D., El-Sayed M.A.. (2013).

32 Lecarme O., Pinedo-Rivera T., Berton K., Berthier J., and Peyrade D. Plasmonic coupling in nondipolar gold collidal dimers. *Applied Physics Letters*, 98, 8 (2011), 083122.

33 Liu Z., Boltasseva A., Pedersen R.H., Bakker R., Kildishev A.V., Drachev V.P., and Shalaev V.M. Plasmonic nanoantenna arrays for the visible. *Metamaterials*, 2 , 1 (2008), 45.

34 Chandra M., Dowgiallo A.M., and Knappenberger Jr K.L. Controlled Plasmon Resonance Properties of Hollow Gold Nanosphere Aggregates. *Journal of the American Chemical Society*, 132, 44 (2010), 15782.

35 Rechberger W., Hohenau A., Leitner A., Krenn J.R., Lamprecht B., Aussenegg F.R. Optical properties of two interacting gold nanoparticles. *Opt. Commun.* , 137, 220 (2003), 1 - 3.

36 Maier S.A., Brongersma M.L., Kik P.G., and Atwater H.A. Observation of near-field coupling in metal nanoparticle chains using far-field polarization spectroscopy. *Phys. Rev. B*, 65 (2002), 193408.

37 Meier M., Wokaun A., and Liao P.F. Enhanced fields on rough surfaces: dipolar interactions among particles of sizes exceeding the Rayleigh limit. *J. Opt. Soc. Am. B*, 2, 6 (1985), 931.

38 Canfield B. K., Kujala S., Kauranen M., Jefimovs K., Vallius T., and Turunen J. (2005).

39 Park D., Stroud S.Y. Surface-plasmon dispersion relations in chains of metallic nanoparticles: An exact quasistatic calculation (2004).

40 Zhao L.L., Kelly K.L., Schatz G.C. The Optical Properties of Metal Nanoparticles: The Influence of Size, Shape, and Dielectric Environment (2003).

41 Zou S., Janel N., Schatz G. Silver nanoparticle array structures that produce remarkably narrow plasmon lineshapes (2004).

42 Haynes C., Yonzon C., Zhang X., Van Duyne R. Surface-enhanced raman sensors: Early history and the development of sensors for quantitative biowarfare agent and glucose detection. Journal Of Raman Spectroscopy (2005).

43 Braun G.B., Friman T., Pang H.B., Pallaoro A., De Mendoza T.H., Willmore A.M.A., Kotamraju V.R., Mann A.P., She Z.G., Sugahara K.N., Reich N.O., Teesalu T., Ruoslahti E. Etchable plasmonic nanoparticle probes to image and quantify cellular internalization (2014).

44 Yeshchenko O.A., Dmitruk I.M., Alexeenko A.A., Losytskyy M.Y., Kotko A. V. , Pinchuk A.O. Size-dependent surface-plasmon-enhanced photoluminescence from silver nanoparticlesembedded in silica (2009).

45 Dulkeith E, Niedereichholz T, Klar TA, Feldmann J, Von Plessen G, Gittins DI, Mayya KS, Caruso F. Plasmon emission in photoexcited gold nanoparticles (2004).

46 Zheng J., Ding Y., Tian B., Zhong L.W., Zhuang X. Luminescent and raman active silver nanoparticles with polycrystalline structure (2008).

47 Zheng J., Petty J. T. , Dickson R. M. High quantum yield blue emission from water-soluble Au8 nanodots (2003).

48 Link S., Beeby A. ,FitzGerald S. ,El-Sayed M. A. ,Schaaff T. G. , Whetten R. L. Visible to Infrared Luminescence from a 28-Atom Gold Cluster (2002).

49 Mohamed MB, Volkov V, Link S, El-Sayed MA. The 'lightning' gold nanorods: Fluorescence enhancement of over a million compared to the gold metal (2000).

50 Varnavski, O. Relative Enhancement of Ultrafast Emission in Gold Nanorods (2003).

51 Lakowicz, Joseph. *Principles of fluorescent spectroscopy*. Springer Science+Business Media, LLC, 2006.

52 Zheng J., Zhang C. , Dickson R. M. Highly Fluorescent,Water-Soluble, Size-Tunable Gold Quantum Dots (2004).

53 Diez I., Ras R.. Fluorescent silver nanoclusters (2011).

54 Mooradian A. Photoluminescence of metals (1969).

55 Braun G. B., Friman T. ,Pang H. , Pallaoro A. , Hurtado de Mendoza T. , Willmore A. A., Kotamraju V. R. ,Mann A. P. , She Zh.,Sugahara K. N. , Reich N. O., Teesalu T. , Ruoslahti E. Etchable plasmonic nanoparticle probes to image and quantify cellular internalization (2014).

56 Lakowicz, Joseph. Radiative Decay Engineering: Biophysical and Biomedical Applications (2001).

57 Geddes C. D., Cao H., Gryczynski I. , Gryczynski Z., Fang J. , Lakowicz J. R. Metal-Enhanced Fluorescence (MEF) Due to Silver Colloids on a Planar Surface: Potential Applications of Indocyanine Green to in Vivo Imaging (2003).

58 Khatua S., Paulo P. M. R. , Yuan H. , Gupta A. , Zijlstra P. , Orrit M. Resonant Plasmonic Enhancement of Single-Molecule Fluorescence by Individual Gold Nanorods (2014).

59 Liu S., Huang L., Li J. ,Wang C. , Li Q. , Xu H. , Guo H., Meng Z. , Shi Zh., Li Zh. Simultaneous Excitation and Emission Enhancement of Fluorescence Assisted by Double Plasmon Modes of Gold Nanorods (2013).

60 Aldossari A., Shannahan J. H. , Podila R. , Brown J. M. Influence of Physicochemical Properties of Silver Nanoparticles on Mast Cell Activation and Degranulation (2015).

61 Gong J., Dai R. ,Wang Z. , Zhang Z. Thickness dispersion of surface plasmon of Ag nnao-thin films: Determination by ellipsometrry iterated with transmittance method. *Scientific Reports*, 5 (2015), 9279.

62 Savitzky A., Golay M. J. (1964).

63 Jain P. K., Lee K. S., El-Sayed I. H., and El-Sayed M. A. (2006).

64 Citrin D.S. Coherent Excitation Transport in Metal−Nanoparticle Chains. *Nano Lett.*, 5, 5 (2005).

65 Anker J. N., Hall W. P., Lyandres O., Shah N. C., Zhao J., and Van Duyne R. P. (2008).

66 Garcia-Parajo M. F. (2008).

67 Nishiuma S., Handa Y., Imamura T., Ogino M., Yamada T., Furusawa K., and Kuroda R. (2008).

68 Lee B., Lee I. M., Kim S., Oh D. H., and Hesselink L. (2010).

69 Sukharev M. and Seideman T. (2007).

70 Guillot N., de la Chapelle M. L. (2012).

71 Chen J., Xu R., Yan Z., Tang C., Chen Z., and Wang Z. (2013).

72 Rand B. P., Peumans P., and Forrest S. R. (2004).

73 Spinelli P., Ferry E., Van De Groep J., Van Lare M., Verschuuren A. , Schropp I., Atwater A., Polman A., Ferry V. E., Verschuuren M. A., Schropp R. E. I., and Atwater. H. A. (2012).

74 Leroux Y., Lacroix J. C. , Fave C. , Stockhausen V. , Felidj N., Grand J., Hohenau A., Krenn J. R. (2009).

75 Wilcoxon J.P., Martin J.E., Parsapour F., Wiedenman B., Kelley D.F. Photoluminescence from nanosize gold clusters (1998).

76 Yeshchenko O.A., Bondarchuk I.S., Losytskyy M.Y. Surface plasmon enhanced photoluminescence from copper nanoparticles: Influence of temperature (2014).

77 Stamplecoskie K.G., Scaiano J.C., Tiwari V.S., Anis H. Optimal size of silver nanoparticles for surface enhanced raman spectroscopy (2011).

78 Brouwer A.M. *Standards for photoluminescence quantum yield measurements in solution (iupac technical report)*. 2213-2228, 2011.

79 Apell P., Monreal R., Lundqvist S. Photoluminescence of noble-metals (1988).

80 Dmitruk I, Blonskiy I, Pavlov I, Yeshchenko O, Alexeenko A, Dmytruk A, Korenyuk P, Kadan V. Surface plasmon as a probe of local field enhancement (2009).

81 Tcherniak A., Dominguez-Medina S., Chang W.S., Swanglap P., Slaughter L.S., Landes C.F., Link S. One photon plasmon luminescence and its application to correlation spectroscopy as a probe for rotational and translational dynamics of gold nanorods (2011).

82 Gaiduk A, Yorulmaz M, Orrit M. Correlated absorption and photoluminescence of single gold nanoparticles (2011).

83 Zhang T., Lu G., Shen H., Shi K., Jiang Y., Xu D., Gong Q. Photoluminescence of a single complex plasmonic nanoparticle (2014).

84 Pilling S., Mendes L.A.V., Bordalo V., Guaman C.F.M., Ponciano C.R., Da Silveira E.F. The influence of crystallinity degree on the glycine decomposition induced by 1 mev proton bombardment in space analog conditions (2013).

85 Futamura Y, Yahara K, Yamamoto K. Evidence for the production of fluorescent pyrazine derivatives using supercritical water (2007).

86 Pinchuk A, Kreibig U. Interface decay channel of particle surface plasmon resonance (2003).

87 Shang L. Engineered nanoparticles interacting with cells: size matters (2011).

88 Verma A., Stellacci F. Effect of surface properties on nanoparticle-cell interactions (2010).

89 Mahmoudi M., Saeedi-Eslami S.N., Shokrgozar M.A., Azadmanesh K., Hassanlou M., Kalhor H.R., Burtea C., Rothen-Rutishauser B., Laurent S., Sheibani S., Vali H. Cell "Vision": Complementary factor of protein corona in nanotoxicology (2012).

90 Verma A, Uzun O, Hu Y, Han HS, Watson N, Chen S, Irvine DJ, Stellacci F. Surface-structureregulated cell-membrane penetration by monolayer-protected nanoparticles (2008).

91 Shang L. Engineered nanoparticles interacting with cells: size matters (2011).

92 Amidzadeh Z., Behbahani A. B., Erfani N. , Sharifzadeh S. , Ranjbaran R. , Moezi L. , Aboualizadeh F. , Okhovat M., Alavi P. , Azarpira N. Assessment of Different Permeabilization Methods of Minimizing Damage to the Adherent Cells for Detection of Intracellular RNA by Flow Cytometry (2014).

93 Kim JS, Kuk E, Yu KN, Kim JH, Park SJ, Lee HJ, Kim SH, Park YK, Park YH, Hwang CY, Kim YK, Lee YS, Jeong DH, Cho MH. Antimicrobial effects of silver nanoparticles (2007).

94 Manshian B.B., Pfeiffer C., Pelaz B., Heimerl T., Gallego M., Möller M., Del Pino P., Himmelreich U., Parak W.J, Soenen S.J. High-content imaging and gene expression approaches to unravel the effect of surface functionality on cellular interactions of silver nanoparticles (2015).

95 Blair J.M.A., Webber M.A., Baylay A.J., Ogbolu D.O., Piddock L.J.V. Molecular mechanisms of antibiotic resistance (2015).

96 Liau S.Y., Read D.C., Pugh W.J., Furr J.R., Russell A.D. Interaction of silver nitrate with readily identifiable groups: Relationship to the antibacterial action of silver ions (1997).

97 Zhang T., Wang L., Chen Q., Chen C. Cytotoxic potential of silver nanoparticles (2014).

98 Yang W., Lee S., Lee J., Bae Y., Kim D. Silver nanoparticle-induced degranulation observed with quantitative phase microscopy (2010).

99 Culhane K.M., Spendier K. , Pinchuk A. O. Functionalized fluorescent silver nanoparticle surfaces for novel sensing and imaging techniques (2015).

100 Culhane K., Jiang K. , Neumann A. , Pinchuk A. O. Laser-Fabricated Plasmonic Nanostructures for Surface-Enhanced Raman Spectroscopy of Bacteria Quorum Sensing Molecules (2017).

101 Raether, H. *Surface Plasmons on Smooth and Rough Surfaces and on Gratings*. Springer-Verlag, Berlin, 1988.

102 Santbergen R., Temple T. L. ,Liang R. , Smets A. H. M. , van Swaaij M. , Zeman M. Application of plasmonic silver island films in thin-film silicon solar cells. *J. of Optics*, 14, 2 (2012), 024010.

103 Jia K., Bijeon J. L. , Adam P. M. , Ionescu R. E. A facile and cost-effective TEM grid aproach to design gold nano-structured substrates for high throughput plasmonic sensitive detection of biomolecules. *Analyst.*, 138 (2013), 1015-1019.

104 Kalyuzhny G., Vaskevich A. ,Schneeweiss M. A. , Rubinstein I. Sensitivity and optimization of localized surface plasmon resonance transducers. *ACS Nano.*, 5 (2011), 748-760.

105 Smith A. M., Duan H. , Mohs A. M., Nie S. Bioconjugated quantum dots for in vivo molecular and cellular imaging. *Adv. Drug Deliv. Rev.*, 60 (2008), 1226-1240.

106 Chen S., Svedendahl M. , Kall M., Gunnarsson , Dmitriev A. Ultrahigh sensitivity made simple: nanoplasmonic label-free biosensing with an extremely low limit-of-detection for bacterial and cancer diagnostics. *Nanotechnology*, 20 (2009), 434015.

107 Sockalingum G. D., Beljebbar A. , Morjani H., Angiboust J. F. , Manfait M. Characterization of island films as surface-enhanced Raman spectroscopy substrates for detecting low antitumor drug concentrations at single cell level. *Biospectroscopy*, 4, S5 (1998), S71-S78.

108 Johnson P. B., Christy R. W. Optical constants of the noble metals. *Phys. Rev. B*, 6, 12 (1972), 4370-4379.

109 Jarrett D. N., Ward L. Optical properties of discontinuous gold films. *J. Phys. D: Appl. Phys.*, 9 (1976), 1515-1527.

110 Norrman S., Andersson T. , Granqvist C. G. , Hunderi O. Optical properties of discontinuous gold films. *Phys. Rev. B*, 18 (1978), 674-694.

111 Norrman S., Andersson T. , Granqvist C. G. Optical absorption in discontinuous gold films. *Solid St. Comm.*, 23, 4 (1977), 261-265.

112 Bohren C. F., Huffman D. R. *Absorption and scattering of light by small particles*. Wiley-Verlag, 2007.

113 Gittleman J. I., Abeles B. Comparison of the effective medium and the Maxwell-Garnett predictions for the dielectric constants of granular metals. *Phys. Rev. B*, 15, 6 (1977), 3273-3275.

114 Tyboroski M. H., Anderson N. R. , Camley R. E. An effective medium study of surface plasmon polaritons in nanostructured gratings using attenuated total reflection (2014).

115 Dmitruk N. L., Fursenko O. V. , Kondratenko O. S. , Romanyuk V. R. Optical characterization of thin Au films by standard and polaritonic ellipsometry. *Semicond. Phys. Quantum Electron. Optoelectron.*, 6, 3 (2003), 349-353.

116 Ferri M., Frasconi F., Mazzei T. Protein immobilization at gold–thiol surfaces and potential for biosensing (2010).

117 Green R. J., Davies J. , Davies M. C. , Roberts C. J. , Tendler S. J. B. Surface plasmon resonance for real time in situ analysis of protein adsorption to polymer surfaces (1997).

118 Reinhard B. M., Siu M., Agarwal H. , Alivisatos A. P., Liphardt J. Calibration of Dynamic Molecular Rulers Based on Plasmon Coupling between Gold Nanoparticles. *NanoLetters* (2005).

119 Mühling M., Bradford A., Readman J.W. An investigation into the effects of silver nanoparticles on antibiotic resistance of naturally occurring bacteria in an estuarine sediment. *Marine Environmental Research* (2009).

120 Lofas S., Johnsson B. A Novel Hydrogel Matrix on Gold Surfaces in Surface Plasmon Resonance Sensors for Fast and Efficient Covalent Immobilization of Ligands. *J. CHEM. SOC., CHEM. COMMUN.*, (1990).

121 Persson B., Stenhag K., Nilsson P., Larsson A., Uhlén M., Nygren P. Analysis of oligonucleotide probe affinities using surface plasmon resonance: a means for mutational scanning. *Anal Biochem* (1997).

122 O'Neal D., Hirsch L., Halas N., Payne J., West J. Photo-thermal tumor ablation in mice using near infrared-absorbing nanoparticles (2004).

123 Lal S., Link S. , Halas N. J. (2007).

124 Brown A. M., Sundararaman R. , Narang P. , Goddard W. A. , Atwater H. A. Nonradiative Plasmon Decay and Hot Carrier Dynamics: Effects of Phonons, Surfaces, and Geometry (2016).

125 Bharadwaj, P. & Novotny, L. Spectral dependence of single molecule fluorescence enhancement (2007).

126 Dragnea B., Chen C. , Kwak E. S. , Stein B. , Kao C. (2003).

127 Sönnichsen C., Reinhard B. M. , Liphardt J. , Alivisatos A. P. (2005).

128 Hogan N. J. Nanoparticles Heat through Light Localization (2014).

129 Gu Y., Li Q. , Xiao J., Wu K. , Wang G. P. *Journal of Applied Physics,* 2 (2011).

APPENDICES

A. SCIENTIFIC PUBLICATIONS OF RESULTS INCLUDED IN THIS DISSERTATION

Table 2. List of publications and the corresponding parts of this dissertation.

Chapter	Refereed Publications, Book Chapter
Chapter 2	**1.** Vira Kravets and Anatoliy Pinchuk, *Near-, middle, and far-field dipolar interactions in gold nanoparticle arrays*, Proceedings of SPIE 9724, Plasmonics in biology and medicine XIII, 97240B, (2016) **2.** Vira Kravets, Leonidas Ocola, Yuriy Khalavka, and Anatoliy Pinchuk, *Polarization and distance dependent coupling in linear chains of gold nanoparticles*, Appl. Phys. Letters, Vol. 106, 5 (2015) **3.** V.V. Kravets, O. A. Yeshchenko, V.V. Gozhenko, L.E. Ocola, D. A. Smith, J.V. Vedral, A.O. Pinchuk, *Electrodynamic coupling in regular arrays of gold nanocylinders*, Journal of Physics D Applied Physics, 45, 045102 (2012)
Chapter 3	**4.** Vira Kravets, Zamawang Almemar, Ke Jiang, Kyle Culhane, Rosa Machado, Guy Hagen, Andriy Kotko, Ihor Dmitruk, Kathrin Spendier, and Anatoliy Pinchuk, *Imaging of biological cells using luminescent silver nanoparticles*, Nanoscale Research Letters, 11:30 (2016) **5.** V.V. Kravets and A.O. Pinchuk, *Surface Plasmon Enhanced Fluorescence of Glycine-Dimer-Functionalized Silver Nanoparticles*, Nano-Optics: Principles Enabling Basic Research and Applications, chapter 20, 405-410, Springer Science+Business Media Dordrecht (2017).
Chapter 4	**6.** Vira V. Kravets, Nicholas R. Anderson, Dario Bueno-Baques, Joshua R. Baptist , Robert E. Camley , Anatoliy O. Pinchuk *Optical properties of gold films of different morphology: Is the effective medium approach effective*, submitted to Journal of Applied Physics

ADDITIONAL PUBLICATIONS

Journal article

E. C. Economou, S. Marinelli, M. C. Smith, A. A. Routt, V. V. Kravets, H. W. Chu, K. Spendier, Z. J. Celinski, *Magnetic, Nanodrug Delivery Through the Mucus Layer of Air-Liquid Interface Cultured Primary Normal Human Tracheobronchial Epithelial Cells*, BioNanoScience, Vol. 6, 3, pp 235-242 (2016).

Contributions to conferences and symposiums

1. V.V. Kravets, Z. Almemar, A. Kotko, I. Dmytruk, A. Pinchuk, *Fluorescent glycine-coated silver nanoparticles as bio-imaging agents for the neural stem cells*, NAP-2014 Proceeding (2015).

2. I. M. Dmituk, S. Z. Malynych, E. S. Grabovskij, V. V. Kravets, and A. O. Pinchuk, *Light scattering by silver nanoparticles in colloidal solutions for improved photovoltaic devices*, Proc. of NAP, vol.3, N202NEA05(3pp) (2014).

3. V.V. Kravets, K. Culhane, I. M. Dmitruk, A. O. Pinchuk, *Glycine-coated photoluminescent silver nanoclusters*, Colloidal Nanocrystals for Biomedical Applications VII, Proc. of SPIE, № 8232, p.8384 (2012).